Electronic Research Archive

https://www.aimspress.com/journal/era

ERA, 34(5): 2774–2804.
DOI: 10.3934/era.2026127
Received: 31 December 2025
Revised: 11 March 2026
Accepted: 18 March 2026
Published: 30 March 2026

Research article

Numerical recovery of unknown source in a kinetic equation with absorption and scattering via an interior measurement

Muhammed Hasdemir[1,*], **İsmet Gölgeleyen**[2] **and Özlem Kaytmaz**[2]

[1] Aydın Vocational School of Health Services, Aydın Adnan Menderes University, Aydın 09020, Türkiye

[2] Department of Mathematics, Faculty of Science, Zonguldak Bülent Ecevit University, Zonguldak 67100, Türkiye

* **Correspondence:** Email: muhammed.hasdemir@adu.edu.tr.

Abstract: This study addresses an inverse source problem for a general stationary kinetic equation involving absorption and scattering terms. The primary objective is the simultaneous reconstruction of the phase space particle distribution and an unknown source in the model, utilizing boundary conditions defined by derivatives and additional interior measurements. In the theoretical part of the study, the uniqueness of the solution to the inverse problem is proved. For the numerical solution, a comprehensive computational framework is developed based on finite difference approximations for derivatives and the trapezoidal rule for the discretization of the integral terms. The reconstruction strategy employs bilinear interpolation techniques coupled with Tikhonov regularization. In addition, a Monte Carlo noise sensitivity analysis is carried out to assess the stability and robustness of the proposed method under perturbed data. Finally, the effectiveness of the method is illustrated through numerical examples.

Keywords: general kinetic equation; inverse source problem; numerical solution; bilinear interpolation; Monte Carlo noise analysis

1. Introduction

In the mathematical modeling of transport phenomena in phase space, kinetic equations form a fundamental class of partial differential equations, describing the evolution of a distribution function depending on both spatial and momentum (or velocity) variables. They arise naturally in a wide range of applications including neutron transport, radiative transfer, plasma physics, semiconductor modeling, and kinetic descriptions of particle dynamics. From a mathematical and physical viewpoint, kinetic formulations provide a systematic framework that bridges microscopic dynamics

with macroscopic observables, a perspective thoroughly developed in foundational and modern works such as [1–3] and more recent analytical surveys [4–6].

Nonequilibrium effects in rarefied gas aerothermodynamics and micro- or nano-scale devices are commonly described using kinetic models, since continuum descriptions are no longer valid and phase space formulations become essential [7–9]. They also play a central role in modeling collisionless and weakly collisional transport in plasma and charged particle systems, including laboratory and space plasmas [10, 11]. In radiation and neutron transport, kinetic equations describe propagation, absorption, and scattering processes in participating media, where boundary-accessible fluxes encode information about volumetric generation and attenuation inside the domain [12–14].

In strongly magnetized plasma environments relevant to fusion devices and astrophysical plasmas, reduced kinetic models such as gyrokinetic equations provide a consistent framework for describing multiscale turbulence and transport phenomena [15, 16]. Phase space approaches are also central to semiclassical and quantum transport theories, where Wigner-type formulations link quantum dynamics with trajectory-based propagation and kinetic limits [17, 18].

Closely related kinetic perspectives also arise in modern materials science and semiconductor physics through charge-carrier transport in complex geometries and heterogeneous media [19, 20]. Further applications include nuclear engineering, where refined kinetic-type models are used to analyze source-related quantities and shielding effects in reactor configurations [21], as well as biological and life science models, where transport-reaction systems with generalized kinetic structures influence collective behavior [22, 23].

From this broad application base, kinetic equations can be viewed as governing the evolution of a phase space distribution function through transport and interaction mechanisms. In particular, when transport is generated by an underlying Hamiltonian flow, the associated stationary operator admits a natural Poisson bracket representation. This geometric structure plays a central role in analytical studies of kinetic equations and provides a natural motivation for the inverse source problem investigated in the present work.

Inverse problems for kinetic equations have been investigated along two main directions: solvability conditions and numerical reconstruction methods, with different choices of boundary conditions and auxiliary information. In [24, 25], the solvability of integral geometry problems and associated inverse problems for transport and kinetic equations are studied by reducing them to Dirichlet-type boundary value problems for third-order partial differential equations. These inverse problems appear to be overdetermined since the entire boundary traces of the solution are prescribed. However, by extending the unknown source function to phase space and imposing a mixed second-order differential relation, the redundant boundary information is naturally balanced. This mechanism converts the problem into a determined one and yields uniqueness, with existence following in several cases.

Inverse problems for transport equations aim to recover an unknown source term and/or medium parameters such as attenuation (absorption) and scattering from measurements performed at the boundary, and they are central in optical and geophysical imaging. A systematic overview of inverse problems for transport equations, emphasizing boundary measurement strategies and reconstruction methods based on integral geometry and microlocal analysis, is provided by [26]. In [27], the authors investigate a coefficient inverse problem for the non stationary single-speed transport equation with lateral boundary observations and an initial condition at $t = 0$, and prove global uniqueness using Carleman estimates. In [28], inverse source and coefficient problems for a first-order transport

equation are investigated and conditional stability estimates are proved under minimal boundary observation data by means of Carleman estimates, while in [29] local Carleman estimates are employed to study inverse coefficient problems and to derive conditional Hölder-type stability results from measurements on a subboundary under suitable geometric assumptions. In [30], the inverse problem of determining the time-independent scattering coefficient or total attenuation in the radiative transport equation is investigated, and global Lipschitz stability together with reverse inequalities is proved via a Carleman estimate with a linear weight.

In [31–33], inverse source and coefficient problems for kinetic equations containing Poisson bracket terms are investigated together with constructive reconstruction strategies, including symbolic algorithms, Galerkin-type schemes, and finite-difference discretizations; the reported numerical experiments indicate stable reconstructions even in the presence of noisy boundary data. For transport equations without scattering and absorption terms, in [34, 35], approximation methods have been developed to compute solutions of overdetermined inverse coefficient problems by reformulating them into determined ones. In [36, 37], hybrid numerical strategies combining finite differences with interpolation or quadrature rules have been proposed for inverse source problems in kinetic and transport equations, accompanied by stability analysis and numerical experiments demonstrating robustness with respect to data perturbations. A recent study [38] addresses an inverse source problem for a stationary kinetic equation with gradient-type boundary data and an interior point observation. In contrast to [38], the present work deals with a kinetic equation involving absorption and scattering terms, employs a boundary condition formulated in terms of $\nabla_x \lambda$ rather than $\nabla_v \lambda$, establishes the uniqueness theorem with proof, uses the trapezoidal rule for the discretization of the scattering term, and includes a detailed error analysis based on additive noise imposed on the boundary data.

Moreover, globally convergent numerical algorithms based on Carleman-weighted convexification techniques have been introduced in [39] for coefficient inverse problems arising in radiative transfer equations, where both attenuation and scattering mechanisms play a crucial role. As another application, in financial mathematics, radial basis function-generated finite difference methods have been employed in [40, 41] for multi dimensional option pricing problems modeled by parabolic partial differential equations, with Gaussian and inverse quadratic kernels yielding high-order convergence rates on both uniform and non uniform meshes.

In the present work, we develop a numerical approach for the inverse problem associated with a general stationary kinetic equation with absorption and scattering terms. In existing works, the direct problem is formulated with boundary traces of the solution (Dirichlet or inflow data), and for the inverse problem the unknown function is typically determined from data prescribed on the outflow part of the boundary. In contrast, the present formulation employs derivative-type boundary information $\nabla u|_{\partial\Omega}$ and $\nabla_x \lambda|_{\partial\Omega}$. Furthermore, the numerical reconstruction relies on this boundary derivative data combined with a single interior measurement $u(x_0, p_0)$, which requires a different solution algorithm.

2. The inverse problem and a uniqueness theorem

In this study, we deal with the following problem in the domain

$$\Omega = \{(x, p) \ : \ x \in D \subset \mathbb{R}^n, \ p \in G \subset \mathbb{R}^n\}.$$

Problem 1. *Find the functions $u(x, p)$ and $\lambda(x, p)$ from the following relations:*

$$Au \equiv \sum_{i=1}^{n} \left(H_{p_i} u_{x_i} - H_{x_i} u_{p_i} \right) + \beta u + I(u) = \lambda(x, p) + F(x, p), \tag{2.1}$$

$$\nabla u|_{\partial\Omega} = u_0, \quad \nabla_x \lambda|_{\partial\Omega} = \lambda_0, \tag{2.2}$$

$$u(x_0, p_0) = u_1, \tag{2.3}$$

where

$$I(u) = \int_G K(x, p, p')\, u(x, p')\, dp'.$$

Here, the variable x denotes the spatial coordinate and p is the velocity variable. The function $u(x, p)$ represents the stationary phase space density of particles at position x with velocity p. $H(x, p)$ is the Hamiltonian function, $\beta(x, p)$ denotes the absorption coefficient, and $K(x, p, p')$ is a scattering kernel. The term $F(x, p)$ collects all known contributions to the right-hand side of the kinetic equation, such as prescribed external sources or modeled collision effects. Finally, the functions $H(x, p)$, $\beta(x, p)$, $K(x, p, p')$, and $F(x, p)$ are given, but the solution $u(x, p)$ and source term $\lambda(x, p)$ are unknown.

Moreover, assume that the function $\lambda(x, p)$ satisfies the following differential equation:

$$\widehat{A}\lambda \equiv \sum_{i=1}^{n} \frac{\partial^2 \lambda}{\partial p_i \partial x_i} = 0. \tag{2.4}$$

Remark 1. *The technical assumption (2.4) imposed on the source term is not introduced arbitrarily. It follows the general solvability scheme developed by Amirov [24], in which an overdetermined inverse problem is transformed into a determined one by extending the admissible class of unknown functions.*

Allowing the unknown function $\lambda(x, p)$ to depend arbitrarily on both x and p leads to an underdetermined problem, and nonuniqueness examples can be readily constructed. To avoid this difficulty, a specific dependence on the variable p is imposed through an additional differential constraint of the form $\hat{A}\lambda = 0$.

In the present work, the condition (2.4) plays precisely this role. It ensures that Problem 1 becomes determined and allows the uniqueness result to be established. Without such a structural restriction, the inverse problem would generally remain underdetermined, and uniqueness could not be expected.

We establish the uniqueness of the solution to Problem 1 in the following theorem. The proof is based on a method similar to that used in Amirov [24]; however, the equation considered here is more general, and the boundary condition prescribed for the unknown source function differs from that in Amirov [24].

Theorem 1. *Let $H(x, p) \in C^2\left(\overline{\Omega}\right)$, $\beta(x, p) \in C^1\left(\overline{\Omega}\right)$, $K(x, p, p') \in C^1\left(\overline{D} \times \overline{G} \times \overline{G}\right)$, and the inequalities*

$$\sum_{i,j=1}^{n} \frac{\partial^2 H}{\partial p_i \partial p_j} \xi^i \xi^j \geq \alpha_1 |\xi|^2, \ \sum_{i,j=1}^{n} \frac{\partial^2 H}{\partial x_i \partial x_j} \xi^i \xi^j \leq -\alpha_2 |\xi|^2, \ (\alpha_1, \alpha_2 > 0), \tag{2.5}$$

hold for all $\xi \in \mathbb{R}^n$, $(x, p) \in \overline{\Omega}$. *Moreover, we assume that*

$$(\alpha_1 - |\beta| - |M_0| - M_3) > \gamma_1,\ (\alpha_2 - |\beta| - M_1 - 2) > \gamma_2,\ (\gamma_1, \gamma_2 > 0), \tag{2.6}$$

where α_1 *and* α_2 *are positive constants and* $M_0 = \max\limits_{1\le j\le n}\left\{\max\limits_{(x,p)\in\overline{\Omega}}\left|\beta_{x_j}\right|\right\}$, $M_1 = M_0C$, $M_2 = \max\limits_{1\le j\le n}\left\{\max\limits_{x\in\overline{D}}\left\{\int\limits_G\int\limits_G K^2(x,p,p')dp'dp, \int\limits_G\int\limits_G K^2_{x_j}(x,p,p')dpdp'\right\}\right\}$, $M_3 = M_2C$, *and* C *is a constant which depends on the domain* Ω. *Then, Problem 1 has at most one solution* (u, λ) *such that* $u, \lambda \in C^2\left(\overline{\Omega}\right)$.

Proof. We prove the theorem by means of the Fredholm alternative theorem and show that the related homogeneous problem, that is $F = u_0 = \lambda_0 = u_1 = 0$, has only the trivial solution. It can be easily verified that

$$\begin{aligned}
2\sum_{j=1}^{n}\frac{\partial u}{\partial p_j}\frac{\partial}{\partial x_j}(Au) &= \sum_{i,j=1}^{n}\left(\frac{\partial^2 H}{\partial p_i\partial p_j}\frac{\partial u}{\partial x_i}\frac{\partial u}{\partial x_j} - \frac{\partial^2 H}{\partial x_i\partial x_j}\frac{\partial u}{\partial p_i}\frac{\partial u}{\partial p_j}\right) + 2\sum_{j=1}^{n}\left(\beta\frac{\partial u}{\partial x_j}\frac{\partial u}{\partial p_j} + \frac{\partial\beta}{\partial x_j}\frac{\partial u}{\partial p_j}u\right)\\
&\quad +2\sum_{j=1}^{n}\int\limits_G K_{x_j}(x,p,p')u(x,p')\,dp'\frac{\partial u}{\partial p_j} + 2\sum_{j=1}^{n}\int\limits_G K(x,p,p')\frac{\partial u}{\partial x_j}dp'\frac{\partial u}{\partial p_j}\\
&\quad +\sum_{i,j=1}^{n}\frac{\partial}{\partial x_j}\left(\frac{\partial u}{\partial p_j}\left(\frac{\partial u}{\partial x_i}\frac{\partial H}{\partial p_i} - \frac{\partial u}{\partial p_i}\frac{\partial H}{\partial x_i}\right)\right) - \sum_{i,j=1}^{n}\frac{\partial}{\partial p_j}\left(\frac{\partial u}{\partial x_j}\left(\frac{\partial u}{\partial x_i}\frac{\partial H}{\partial p_i} - \frac{\partial u}{\partial p_i}\frac{\partial H}{\partial x_i}\right)\right)\\
&\quad +\sum_{i,j=1}^{n}\left(\frac{\partial}{\partial x_i}\left(\frac{\partial H}{\partial p_i}\frac{\partial u}{\partial x_j}\frac{\partial u}{\partial p_j}\right) - \frac{\partial}{\partial p_i}\left(\frac{\partial H}{\partial x_i}\frac{\partial u}{\partial x_j}\frac{\partial u}{\partial p_j}\right)\right)\\
&= 2\sum_{j=1}^{n}\frac{\partial}{\partial p_j}\left(u\frac{\partial\lambda}{\partial x_j}\right).
\end{aligned} \tag{2.7}$$

Integrating (2.7) over Ω and using homogeneous boundary data (2.2) and (2.3), we obtain

$$\begin{aligned}
&\sum_{i,j=1}^{n}\int\limits_\Omega\left(\frac{\partial^2 H}{\partial p_i\partial p_j}\frac{\partial u}{\partial x_i}\frac{\partial u}{\partial x_j} - \frac{\partial^2 H}{\partial x_i\partial x_j}\frac{\partial u}{\partial p_i}\frac{\partial u}{\partial p_j}\right)d\Omega\\
&+2\sum_{j=1}^{n}\int\limits_\Omega\left(\beta\frac{\partial u}{\partial x_j}\frac{\partial u}{\partial p_j} + \frac{\partial\beta}{\partial x_j}\frac{\partial u}{\partial p_j}u\right)d\Omega\\
&+2\sum_{j=1}^{n}\int\limits_\Omega\int\limits_G K_{x_j}(x,p,p')u(x,p')\,dp'\frac{\partial u}{\partial p_j}d\Omega\\
&+2\sum_{j=1}^{n}\int\limits_\Omega\int\limits_G K(x,p,p')\frac{\partial u}{\partial x_j}dp'\frac{\partial u}{\partial p_j}d\Omega = 0.
\end{aligned} \tag{2.8}$$

Using the identity $2ab \leq a^2 + b^2$, the Cauchy–Schwarz inequality and the Poincaré-Wirtinger inequality with $u(x_{0,}p_0) = 0$, the left-hand side of (2.8) can be estimated as follows:

$$
\begin{aligned}
&2\sum_{j=1}^{n}\int_{\Omega}\left(\beta\frac{\partial u}{\partial x_j}\frac{\partial u}{\partial p_j}+\frac{\partial \beta}{\partial x_j}\frac{\partial u}{\partial p_j}u\right)d\Omega \geq \sum_{j=1}^{n}\int_{\Omega}\left(-|\beta|\left(u_{x_j}^2+u_{p_j}^2\right)-\left|\beta_{x_j}\right|\left(u_{p_j}^2+u^2\right)\right)d\Omega\\
&\geq \int_{\Omega}\left(\left(-|\beta|-|M_1|\right)|\nabla_x u|^2+\left(-|\beta|-M_0\right)\left|\nabla_p u\right|^2\right)d\Omega, \qquad (2.9)
\end{aligned}
$$

where $M_0 = \max\limits_{1\leq j\leq n}\left\{\max\limits_{(x,p)\in\overline{\Omega}}\left|\beta_{x_j}\right|\right\}$, $M_1 = M_0C$, and C is a constant which depends on the domain Ω, and

$$
\begin{aligned}
&2\sum_{j=1}^{n}\int_{\Omega}\int_{G}K_{x_j}(x,p,p')u(x,p')\,dp'\frac{\partial u}{\partial p_j}d\Omega+2\sum_{j=1}^{n}\int_{\Omega}\int_{G}K(x,p,p')\frac{\partial u}{\partial x_j}dp'\frac{\partial u}{\partial p_j}d\Omega\\
\geq\ &-\sum_{j=1}^{n}\int_{\Omega}\left(\left(\int_{G}K_{x_j}(x,p,p')u(x,p')\,dp'\right)^2+\left(\frac{\partial u}{\partial p_j}\right)^2\right)d\Omega\\
&-\sum_{j=1}^{n}\int_{\Omega}\left(\left(\int_{G}K(x,p,p')\frac{\partial u}{\partial x_j}dp'\right)^2+\left(\frac{\partial u}{\partial p_j}\right)^2\right)d\Omega\\
\geq\ &-\sum_{j=1}^{n}\int_{D}\int_{G}\left(\int_{G}K_{x_j}^2(x,p,p')dp'\int_{G}u^2(x,p')\,dp'\right)dpdx-\sum_{j=1}^{n}\int_{\Omega}\left(\frac{\partial u}{\partial p_j}\right)^2d\Omega\\
&-\sum_{j=1}^{n}\int_{D}\int_{G}\left(\int_{G}K^2(x,p,p')dp'\int_{G}\left(\frac{\partial u}{\partial x_j}\right)^2dp'\right)dpdx-\sum_{j=1}^{n}\int_{\Omega}\left(\frac{\partial u}{\partial p_j}\right)^2d\Omega\\
=\ &-\sum_{j=1}^{n}\int_{D}\left(\int_{G}u^2(x,p')\,dp'\int_{G}\int_{G}K_{x_j}^2(x,p,p')dp'dp\right)dx-\int_{\Omega}\left|\nabla_p u\right|^2d\Omega\\
&-\sum_{j=1}^{n}\int_{D}\left(\int_{G}\left(\frac{\partial u}{\partial x_j}\right)^2dp'\int_{G}\int_{G}K^2(x,p,p')dp'dp\right)dx-\int_{\Omega}\left|\nabla_p u\right|^2d\Omega\\
\geq\ &-M_3\int_{\Omega}|\nabla_x u|^2\,d\Omega-2\int_{\Omega}\left|\nabla_p u\right|^2d\Omega, \qquad (2.10)
\end{aligned}
$$

where $M_3 = M_2C$ and $M_2 = \max\limits_{1\leq j\leq n}\left\{\max\limits_{x\in\overline{D}}\left\{\int_G\int_G K^2(x,p,p')dp'dp, \int_G\int_G K_{x_j}^2(x,p,p')dpdp'\right\}\right\}$.

Hence, by (2.5), we obtain

$$
\begin{aligned}
0 &\geq (\alpha_1 - |\beta| - |M_0| - M_3) \int_\Omega |\nabla_x u|^2 \, d\Omega + (\alpha_2 - |\beta| - M_1 - 2) \int_\Omega \left|\nabla_p u\right|^2 d\Omega \\
&\geq \gamma \int_\Omega |\nabla u|^2 \, d\Omega, \qquad (2.11)
\end{aligned}
$$

where $\gamma = \min\{\gamma_1, \gamma_2\}$, $\gamma_1, \gamma_2 > 0$. Thus, we have $|\nabla u|^2 \leq 0$, i.e., $u = C$, where C is a constant. On the other hand, by the additional data $u(x_0, p_0) = 0$, we get $u = 0$. Finally from (2.4), we conclude that $\lambda = 0$. So the proof is completed.

3. Computational procedure for the numerical solution of Problem 1

For a concrete and tractable presentation of the numerical scheme, we consider the one-dimensional case $\Omega = (a, b) \times (c, d)$ with $a, b, c, d \in \mathbb{R}$. Applying the operator $\widehat{A} = \frac{\partial^2}{\partial p \partial x}$ to Eq (2.1) leads to a third-order auxiliary partial differential equation:

$$
\begin{aligned}
&\left(H_{ppx} + \beta_p\right) u_x + H_{pp} u_{xx} + H_p u_{xxp} + \left(\beta_x - H_{xxp}\right) u_p - H_{xx} u_{pp} - H_x u_{pxp} \\
&+\beta_{xp} u + \beta u_{xp} + \int_c^d K_{xp} u dp' + \int_c^d K_p u_x dp' = F_{xp}. \qquad (3.1)
\end{aligned}
$$

We approximate the p'-integrals using the trapezoidal rule (a Newton-Cotes formula of degree 1) on the grid nodes $\{p_\ell\}_{\ell=0}^{J+1}$ over the domain $[c, d]$. The quadrature weights $\{w_\ell\}_{\ell=0}^{J+1}$ are defined as

$$
w_\ell = \begin{cases} \frac{\Delta p}{2}, & \ell = 1 \text{ or } \ell = J + 1 \\ \Delta p, & 2 \leq \ell \leq J \end{cases}.
$$

Thus, the integral terms are approximated as

$$
\int_c^d K_{xp}(x_i, p_j, p') u(x_i, p') \, dp' \approx \sum_{\ell=0}^{N_v} w_\ell (K_{xp})_{i,j,\ell} u_{i,\ell}, \qquad (3.2)
$$

$$
\int_c^d K_p(x_i, p_j, p') \frac{\partial u}{\partial x}(x_i, p') \, dp' \approx \sum_{\ell=0}^{N_v} \frac{w_\ell}{2\Delta x} (K_p)_{i,j,\ell} (u_{i+1,\ell} - u_{i-1,\ell}), \qquad (3.3)
$$

where $(K_p)_{i,j,\ell} = K_p(x_i, p_j, p_\ell)$, and $(K_{xp})_{i,j,\ell} = K_{xp}(x_i, p_j, p_\ell)$. Moreover, I and J are positive integers and $\Delta x = \frac{(b-a)}{(I+1)}$, $\Delta p = \frac{(d-c)}{(J+1)}$ denote the mesh sizes in the x- and p-directions, respectively.

By substituting the integral approximations from (3.2) and (3.3), and employing the central finite-difference formulas in (3.1), we obtain the following discrete form:

$$\left(H_{ppx}+\beta_p\right)_{i,j}\frac{\left(\tilde{u}_{i+1,j}-\tilde{u}_{i-1,j}\right)}{2\Delta x}+\left(H_{pp}\right)_{i,j}\frac{\left(\tilde{u}_{i+1,j}-2\tilde{u}_{i,j}+\tilde{u}_{i-1,j}\right)}{(\Delta x)^2}$$
$$+\left(H_p\right)_{i,j}\frac{\left(2\tilde{u}_{i,j-1}-2\tilde{u}_{i,j+1}+\tilde{u}_{i+1,j+1}+\tilde{u}_{i-1,j+1}-\tilde{u}_{i+1,j-1}-\tilde{u}_{i-1,j-1}\right)}{2(\Delta x)^2(\Delta p)}$$
$$+\left(\beta_x-H_{xxp}\right)_{i,j}\frac{\left(\tilde{u}_{i,j+1}-\tilde{u}_{i,j-1}\right)}{2\Delta p}-(H_{xx})_{i,j}\frac{\left(\tilde{u}_{i,j+1}-2\tilde{u}_{i,j}+\tilde{u}_{i,j-1}\right)}{(\Delta p)^2}$$
$$-(H_x)_{i,j}\frac{\left(2\tilde{u}_{i-1,j}-2\tilde{u}_{i+1,j}+\tilde{u}_{i+1,j+1}-\tilde{u}_{i-1,j+1}+\tilde{u}_{i+1,j-1}-\tilde{u}_{i-1,j-1}\right)}{2(\Delta x)(\Delta p)^2}$$
$$+\left(\beta_{xp}\right)_{i,j}\tilde{u}_{i,j}+(\beta)_{i,j}\frac{\left(\tilde{u}_{i+1,j+1}-\tilde{u}_{i+1,j-1}-\tilde{u}_{i-1,j+1}+\tilde{u}_{i-1,j-1}\right)}{4\,\Delta x\,\Delta p}$$
$$+\sum_{\ell=0}^{J+1}w_\ell\,(K_{xp})_{i,j,\ell}\,\tilde{u}_{i,\ell}+\sum_{\ell=0}^{J+1}\frac{w_\ell}{2\Delta x}\,(K_p)_{i,j,\ell}\,(\tilde{u}_{i+1,\ell}-\tilde{u}_{i-1,\ell})=\left(F_{xp}\right)_{i,j}. \tag{3.4}$$

After simplifications, the resulting discrete equation takes the form:

$$\begin{aligned}\widehat{A}Au=\;&\tilde{u}_{i-1,j-1}\,(-k_1+k_2+k_{10})+\tilde{u}_{i-1,j}\,(-k_5+k_3-2k_2)+\tilde{u}_{i-1,j+1}\,(k_1+k_2-k_{10})+\tilde{u}_{i,j-1}\,(2k_1+k_6-k_4)\\&+\tilde{u}_{i,j}\,(-2k_3+2k_4+k_9)+\tilde{u}_{i,j+1}\,(-2k_1-k_6-k_4)+\tilde{u}_{i+1,j-1}\,(-k_1-k_2-k_{10})+\tilde{u}_{i+1,j}\,(k_5+k_3+2k_2)\\&+\tilde{u}_{i+1,j+1}\,(k_1-k_2+k_{10})+\sum_{\ell=0}^{J+1}k_7(i,j,\ell)\,\tilde{u}_{i,\ell}+\sum_{\ell=0}^{J+1}k_8(i,j,\ell)\;(\tilde{u}_{i+1,\ell}-\tilde{u}_{i-1,\ell})=\left(F_{xp}\right)_{i,j},\end{aligned} \tag{3.5}$$
$$i=1,\ldots,I,\ j=1,\ldots,J,\ \ell=0,...,J+1,$$

where the coefficients

$$k_1(i,j)=\frac{\left(H_p\right)_{i,j}}{2(\Delta x)^2(\Delta p)},\ k_2(i,j)=\frac{(H_x)_{i,j}}{2(\Delta x)(\Delta p)^2},\ k_3(i,j)=\frac{\left(H_{pp}\right)_{i,j}}{(\Delta x)^2},\ k_4(i,j)=\frac{(H_{xx})_{i,j}}{(\Delta p)^2}$$
$$k_5(i,j)=\frac{\left(H_{ppx}+\beta_p\right)_{i,j}}{2\Delta x},\ k_6(i,j)=\frac{\left(-\beta_x+H_{xxp}\right)_{i,j}}{2\Delta p},\ k_7(i,j,\ell)=w_\ell\,(K_{xp})_{i,j,\ell},$$
$$k_8(i,j,\ell)=\frac{w_\ell}{2\Delta x}\,(K_p)_{i,j,\ell},k_9(i,j)=\left(\beta_{xp}\right)_{i,j},\ k_{10}(i,j)=\frac{(\beta)_{i,j}}{4\Delta x\Delta p}. \tag{3.6}$$

The treatment of the boundary conditions in the finite-difference scheme is based on the following approximations:

$$\tilde{u}_x(a,p)\approx\frac{-3\tilde{u}_{0,j}+4\tilde{u}_{1,j}-\tilde{u}_{2,j}}{2\Delta x}=g_L\left(p_j\right),\quad \tilde{u}_x(b,p)\approx\frac{3\tilde{u}_{I+1,j}-4\tilde{u}_{I,j}+\tilde{u}_{I-1,j}}{2\Delta x}=g_R\left(p_j\right),$$
$$\tilde{u}_p(x,c)\approx\frac{-3\tilde{u}_{i,0}+4\tilde{u}_{i,1}-\tilde{u}_{i,2}}{2\Delta p}=h_B\left(x_i\right),\quad \tilde{u}_p(x,d)\approx\frac{3\tilde{u}_{i,J+1}-4\tilde{u}_{i,J}+\tilde{u}_{i,J-1}}{2\Delta p}=h_T\left(x_i\right),$$
$$i=1,\ldots,I+1,\ j=1,\ldots,J+1.$$

At the $I \times J$ mesh points of Ω, the approximate solution $\tilde{u}_{i,j}$ of Problem 1 is determined by solving the matrix equation:

$$\Lambda\widetilde{\mathbf{u}} + \mathbf{b} = \mathbf{G}, \tag{3.7}$$

where Λ is a block tridiagonal banded matrix. For convenience, we decompose the coefficient matrix as

$$\Lambda = \Lambda_1 + \Lambda_2 + \Lambda_3,$$

where Λ_1 and Λ_2 are block tridiagonal matrices in $\mathbb{R}^{IJ\times IJ}$ of the form

$$\Lambda_1 = \begin{bmatrix} \mathcal{M}_1^{(1)} & \mathcal{M}_2^{(1)} & 0 & \cdots & 0 \\ \mathcal{M}_3^{(2)} & \mathcal{M}_1^{(2)} & \mathcal{M}_2^{(2)} & \ddots & \vdots \\ 0 & \mathcal{M}_3^{(3)} & \ddots & \ddots & 0 \\ \vdots & \ddots & \ddots & \ddots & \mathcal{M}_2^{(I-1)} \\ 0 & \dots & 0 & \mathcal{M}_3^{(I)} & \mathcal{M}_1^{(I)} \end{bmatrix}_{IJ\times IJ}, \tag{3.8}$$

$$\Lambda_2 = \begin{bmatrix} \mathcal{M}_4^{(1)} & \mathcal{M}_5^{(1)} & 0 & \cdots & 0 \\ -\mathcal{M}_5^{(2)} & \mathcal{M}_4^{(2)} & \mathcal{M}_5^{(2)} & \ddots & \vdots \\ 0 & -\mathcal{M}_5^{(3)} & \ddots & \ddots & 0 \\ \vdots & \ddots & \ddots & \ddots & \mathcal{M}_5^{(I-1)} \\ 0 & \dots & 0 & -\mathcal{M}_5^{(I)} & \mathcal{M}_4^{(I)} \end{bmatrix}_{IJ\times IJ}. \tag{3.9}$$

Here, for each $i = 1, \dots, I$, we define $M_1^{(i)}, M_2^{(i)}, M_3^{(i)} \in \mathbb{R}^{J\times J}$ by

$$M_1^{(i)} = \begin{bmatrix} f_1(i,1) & f_2(i,1) & 0 & \cdots & 0 \\ f_3(i,2) & f_1(i,2) & f_2(i,2) & \ddots & \vdots \\ 0 & \ddots & \ddots & \ddots & 0 \\ \vdots & \ddots & f_3(i,J-1) & f_1(i,J-1) & f_2(i,J-1) \\ 0 & \cdots & 0 & f_3(i,J) & f_1(i,J) \end{bmatrix}_{J\times J}, \tag{3.10}$$

$$M_2^{(i)} = \begin{bmatrix} f_4(i,1) & f_5(i,1) & 0 & \cdots & 0 \\ f_6(i,2) & f_4(i,2) & f_5(i,2) & \ddots & \vdots \\ 0 & \ddots & \ddots & \ddots & 0 \\ \vdots & \ddots & f_6(i,J-1) & f_4(i,J-1) & f_5(i,J-1) \\ 0 & \cdots & 0 & f_6(i,J) & f_4(i,J) \end{bmatrix}_{J\times J}, \tag{3.11}$$

$$M_3^{(i)} = \begin{bmatrix} f_7(i,1) & f_8(i,1) & 0 & \cdots & 0 \\ f_9(i,2) & f_7(i,2) & f_8(i,2) & \ddots & \vdots \\ 0 & \ddots & \ddots & \ddots & 0 \\ \vdots & \ddots & f_9(i,J-1) & f_7(i,J-1) & f_8(i,J-1) \\ 0 & \cdots & 0 & f_9(i,J) & f_7(i,J) \end{bmatrix}_{J\times J}, \tag{3.12}$$

where

$$
\begin{aligned}
f_1(i,j) &= -2k_3(i,j) + 2k_4(i,j) + k_9(i,j), & f_2(i,j) &= -2k_1(i,j) - k_6(i,j) - k_4(i,j),\\
f_3(i,j) &= \ 2k_1(i,j) + k_6(i,j) - k_4(i,j), & f_4(i,j) &= \ k_5(i,j) + k_3(i,j) + 2k_2(i,j),\\
f_5(i,j) &= \ k_1(i,j) - k_2(i,j) + k_{10}(i,j), & f_6(i,j) &= -k_1(i,j) - k_2(i,j) - k_{10}(i,j),\\
f_7(i,j) &= -k_5(i,j) + k_3(i,j) - 2k_2(i,j), & f_8(i,j) &= k_1(i,j) + k_2(i,j) - k_{10}(i,j),\\
f_9(i,j) &= -k_1(i,j) + k_2(i,j) + k_{10}(i,j).
\end{aligned}
$$

The integral contributions yield dense matrices $M_4^{(i)}, M_5^{(i)} \in \mathbb{R}^{J\times J}$ defined entrywise by

$$
\mathcal{M}_4^{(i)} = \begin{bmatrix} k_7(i,1,1) & k_7(i,1,2) & \cdots & k_7(i,1,J) \\ k_7(i,2,1) & k_7(i,2,2) & \cdots & k_7(i,2,J) \\ \vdots & \vdots & \ddots & \vdots \\ k_7(i,J,1) & k_7(i,J,2) & \cdots & k_7(i,J,J) \end{bmatrix},\ \mathcal{M}_5^{(i)} = \begin{bmatrix} k_8(i,1,1) & k_8(i,1,2) & \cdots & k_8(i,1,J) \\ k_8(i,2,1) & k_8(i,2,2) & \cdots & k_8(i,2,J) \\ \vdots & \vdots & \ddots & \vdots \\ k_8(i,J,1) & k_8(i,J,2) & \cdots & k_8(i,J,J) \end{bmatrix}.
$$

To incorporate the nonhomogeneous boundary data into the finite-difference scheme, we eliminate the ghost-node values by using second-order one-sided formulas for the normal derivatives. More precisely, for $j = 1,\dots,J$ and $i = 1,\dots,I$, we use

$$
\tilde{u}_x(a,p_j) \approx \frac{-3\tilde{u}_{0,j} + 4\tilde{u}_{1,j} - \tilde{u}_{2,j}}{2\Delta x} = g_L(p_j) \quad \Longrightarrow \quad \tilde{u}_{0,j} = \frac{4\tilde{u}_{1,j} - \tilde{u}_{2,j} - 2\Delta x\, g_L(p_j)}{3}, \tag{3.13}
$$

$$
\tilde{u}_x(b,p_j) \approx \frac{3\tilde{u}_{I+1,j} - 4\tilde{u}_{I,j} + \tilde{u}_{I-1,j}}{2\Delta x} = g_R(p_j) \quad \Longrightarrow \quad \tilde{u}_{I+1,j} = \frac{4\tilde{u}_{I,j} - \tilde{u}_{I-1,j} + 2\Delta x\, g_R(p_j)}{3}, \tag{3.14}
$$

$$
\tilde{u}_p(x_i,c) \approx \frac{-3\tilde{u}_{i,0} + 4\tilde{u}_{i,1} - \tilde{u}_{i,2}}{2\Delta p} = h_B(x_i) \quad \Longrightarrow \quad \tilde{u}_{i,0} = \frac{4\tilde{u}_{i,1} - \tilde{u}_{i,2} - 2\Delta p\, h_B(x_i)}{3}, \tag{3.15}
$$

$$
\tilde{u}_p(x_i,d) \approx \frac{3\tilde{u}_{i,J+1} - 4\tilde{u}_{i,J} + \tilde{u}_{i,J-1}}{2\Delta p} = h_T(x_i) \quad \Longrightarrow \quad \tilde{u}_{i,J+1} = \frac{4\tilde{u}_{i,J} - \tilde{u}_{i,J-1} + 2\Delta p\, h_T(x_i)}{3}. \tag{3.16}
$$

Substituting (3.13)–(3.16) into the discrete equations eliminates all boundary unknowns and yields a linear system involving only the interior nodal values $\tilde{u}_{i,j}$, $i = 1,\dots,I$, $j = 1,\dots,J$. All the terms containing the prescribed boundary data g_L, g_R, h_B, and h_T are transferred to the right-hand side and collected in the vector $\mathbf{b}$ in (3.7). The same elimination procedure is applied to the corner ghost nodes (e.g., $\tilde{u}_{0,0}$, $\tilde{u}_{0,J+1}$, $\tilde{u}_{I+1,0}$, $\tilde{u}_{I+1,J+1}$) by successive use of (3.13)–(3.16). Consequently, the coefficient matrix Λ in (3.7) already incorporates the boundary conditions through these substitutions. In particular, in the decomposition $\Lambda = \Lambda_1 + \Lambda_2 + \Lambda_3$, the matrix Λ_3 collects the additional coefficient corrections generated by the boundary elimination, whereas $\mathbf{b}$ accounts for the resulting nonhomogeneous boundary conditions.

Assume that an interior measurement of u is available at the point $(x_0, p_0) \in \Omega$, and let (i^*, j^*) be the corresponding grid indices (i.e., $x_{i^*} = x_0$ and $p_{j^*} = p_0$). We impose this information by replacing one equation in the linear system with the constraint

$$
\tilde{u}_{i^*,j^*} = u_1. \tag{3.17}
$$

The numerical solution vector is represented by $\widetilde{\mathbf{u}} \in \mathbb{R}^{IJ}$, which denotes the vector of unknowns at the interior grid points. For instance,

$$
\widetilde{\mathbf{u}} = \left[\tilde{u}_{1,1}, \tilde{u}_{1,2}, ..., \tilde{u}_{1,J}, \tilde{u}_{2,1}, \tilde{u}_{2,2}, ..., \tilde{u}_{2,J}, ..., \tilde{u}_{I,1}, \tilde{u}_{I,2}, ..., \tilde{u}_{I,J}\right]^T.
$$

If $r = \mathrm{ind}(i^*, j^*)$ is the position of $\tilde{u}_{i^*,j^*}$ in $\widetilde{\mathbf{u}}$, then the replacement is implemented by setting the r-th row of Λ and $\mathbf{G} - \mathbf{b}$ as

$$\Lambda_{r,:} = 0, \qquad \Lambda_{r,r} = 1, \qquad (\mathbf{G} - \mathbf{b})_r = u_1,$$

so that (3.17) holds exactly in the computed solution. Moreover, when the quadrature indices include $\ell = 0$ and $\ell = J + 1$, the boundary values $u_{i,0}$ and $u_{i,J+1}$ arising in the integral terms are eliminated using (3.15)–(3.16) and their contributions are added to $\mathbf{b}$.

In (3.7), the right-hand side $\mathbf{G}$ is a column vector given by

$$\mathbf{G} = [G_{1,1}, G_{1,2}, ..., G_{1,J}, G_{2,1}, G_{2,2}, ..., G_{2,J}, ..., G_{I,1}, G_{I,2}, ..., G_{I,J}]^T,$$

where $G_{i,j} = F_{xp}(x_i, p_j)$ for $i = 1, \ldots, I$ and $j = 1, \ldots, J$.

Having computed the numerical solution $\tilde{u}$, we first define the preliminary approximation $\lambda^{\mathrm{pre}}(x, p)$ by

$$\lambda^{\mathrm{pre}}(x, p) = \{H, \tilde{u}\} - F(x, p) + \beta(x, p)\tilde{u}(x, p) + I(\tilde{u}).$$

Then, the final approximation $\tilde{\lambda}(x, p)$ is reconstructed under the theoretical conditions

$$\frac{\partial^2 \lambda}{\partial p\, \partial x} = 0, \qquad \left.\frac{\partial \lambda}{\partial x}\right|_{x=a} = \lambda_0(a, p), \qquad \left.\frac{\partial \lambda}{\partial x}\right|_{x=b} = \lambda_0(b, p).$$

The reconstruction procedure proceeds as follows:

First, to reconstruct the continuous solution locally, we consider an arbitrary cell indexed by (i, j) in the computational grid. To reconstruct the solution continuously within each cell (i, j), we fit a bilinear surface of the form

$$P(x, p) = a_0 + a_1 x + a_2 p + a_3 xp$$

to the four corner values $\tilde{u}_{i,j}$, $\tilde{u}_{i+1,j}$, $\tilde{u}_{i,j+1}$, $\tilde{u}_{i+1,j+1}$. The partial derivatives of $\tilde{u}$ at the cell center are then approximated by the analytically computed derivatives of P:

$$\tilde{u}_x \approx \frac{\partial P}{\partial x}(x, p) \quad \text{and} \quad \tilde{u}_p \approx \frac{\partial P}{\partial p}(x, p).$$

These values provide a robust approximation of $\tilde{u}_x$ and $\tilde{u}_p$ at the cell centers. The integral term $I(\tilde{u})$ represents a nonlocal dependency and is computed numerically using a quadrature rule with weights w_k. Since the kernel $K(x, p, p')$ is general, we perform this calculation as a matrix-vector summation for each spatial node x_i:

$$I(\tilde{u})_{i,j} \approx \sum_{k=1}^{J+1} w_k K(x_i, p_j, p_k)\tilde{u}_{i,k}.$$

This discrete integral field is then interpolated to the cell centers (x, p) to match the grid location of the derivatives. Finally, combining the derivatives, the reaction term $\beta\tilde{u}$, and the computed integral term, we construct the observed source function values at each cell center:

$$\lambda^{\mathrm{pre}}_{i,j} = \left(H_p \tilde{u}_x - H_x \tilde{u}_p\right)_{i,j} + (\beta\tilde{u})_{i,j} + I(\tilde{u})_{i,j} - F_{i,j}.$$

Since $\lambda_{xp} = 0$ holds in Ω by assumption, the source function admits the additive separated representation $\lambda(x, p) = \rho(x) + \mu(p)$. The reconstruction of $\tilde{\lambda}$ therefore reduces to determining the

univariate functions $\rho(x)$ and $\mu(p)$ independently. In the discrete setting, these are represented by the nodal vectors $\rho_i \approx \rho(x_i)$ and $\mu_j \approx \mu(p_j)$, so that the source term is approximated at each grid point (x_i, p_j) by $\tilde{\lambda}_{ij} \approx \rho_i + \mu_j$.

Incorporating the theoretical model $\lambda(x, p) = \rho(x) + \mu(p)$ together with all additional constraints, we arrive at the large linear system

$$\mathbf{Tz} \approx \mathbf{y},$$

where $\mathbf{z} = [\rho_1, \ldots, \rho_I, \mu_1, \ldots, \mu_J]^T$ collects all unknowns. The matrix $\mathbf{T}$ and the right-hand side vector $\mathbf{y}$ are assembled from the following three sets of equations:

(i) For each cell center defined by indices (i, j), we impose consistency between the nodal unknowns and the source term computed previously (denoted here as $\lambda_{i,j}^{\text{pre}}$):

$$\frac{\rho_i + \rho_{i+1}}{2} + \frac{\mu_j + \mu_{j+1}}{2} \approx \lambda_{i,j}^{\text{pre}}.$$

This guarantees that the reconstructed surface agrees with the information derived from the numerical solution $\tilde{u}$.

(ii) Since $\lambda_x = \rho'(x)$, we impose boundary conditions directly on the vector ρ. We utilize a forward difference at the lower boundary (x_{min}) and a backward difference at the upper boundary (x_{max}):

$$\frac{\rho_2 - \rho_1}{\Delta x} \approx \lambda_0(x_{min}), \quad \frac{\rho_I - \rho_{I-1}}{\Delta x} \approx \lambda_0(x_{max}).$$

(iii) To stabilize the inversion against discretization errors and data noise, we augment the system with a Tikhonov regularization term that promotes smoothness of the reconstructed profiles. This is enforced through the discrete second-order difference constraints

$$\rho_{i+1} - 2\rho_i + \rho_{i-1} \approx 0, \qquad \mu_{j+1} - 2\mu_j + \mu_{j-1} \approx 0$$

for interior indices $2 \le i \le I - 1$ and $2 \le j \le J - 1$, which penalize curvature in ρ and μ and correspond to the standard second-order Tikhonov regularization for discrete inverse problems [42]. Similar regularization strategies have proven effective in related inverse problems arising in porous media and diffusion equations [43, 44].

The regularization parameter α controls the trade-off between data fidelity and solution smoothness. To select α in a principled and data-driven manner, we employ the L-curve criterion [45]. The resulting L-curves and the identified corners for the examples considered in Section 4 are presented there.

The augmented linear system $\mathbf{Tz} = \mathbf{y}$, which incorporates the data fidelity, boundary, and Tikhonov regularization constraints, is solved to obtain the coefficient vector $\mathbf{z}$. The discrete profiles ρ_i and μ_j are then extracted from $\mathbf{z}$, and the regularized source function is reconstructed at each grid point via

$$\tilde{\lambda}(x_i, p_j) = \rho_i + \mu_j.$$

3.1. Error analysis

This subsection summarizes the main error sources inherent in the forward numerical solution of $u(x, p)$ and the subsequent inverse reconstruction of the source function $\lambda(x, p)$.

The finite-difference scheme in (3.4) and (3.5) employs second-order central differences for interior derivatives and second-order one-sided formulas at the boundaries. Under standard

smoothness assumptions on the exact solution u and the coefficients H and β, the local truncation error of the differential operator is of order $O(\Delta x^2 + \Delta p^2)$. The nonlocal integral terms are approximated using the composite trapezoidal rule (3.2) and (3.3); for sufficiently smooth integrands with respect to p', the quadrature error contributes an additional $O(\Delta p^2)$ term. Consequently, assuming stability of the discrete scheme, the numerical solution is expected to converge with an overall rate of $O(\Delta x^2 + \Delta p^2)$, up to problem-dependent constants associated with the kernel and coefficient regularity. Moreover, the elimination of ghost nodes via (3.13)–(3.16) maintains second-order boundary accuracy (in the truncation-error sense) while transferring the effect of nonhomogeneous boundary data into the right-hand side vector $\mathbf{b}$.

The observed convergence rate (CR), also known as the experimental order of convergence, is estimated by comparing two consecutive grid levels with mesh sizes h_k and h_{k+1}, where $h = \max\{\Delta x, \Delta p\}$:

$$\mathrm{CR} \approx \frac{\log\left(\|e\|^{(h_k)}/\|e\|^{(h_{k+1})}\right)}{\log(h_k/h_{k+1})}. \tag{3.18}$$

On sufficiently fine grids, this estimate is expected to be close to 2, consistent with the formal accuracy $O(\Delta x^2 + \Delta p^2)$.

In the numerical experiments, we quantify the forward solver's accuracy using the following discrete relative errors:

$$\|e\|_{2,\mathrm{rel}} = \frac{\left(\sum_{i=1}^{I}\sum_{j=1}^{J}|\tilde{u}_{i,j} - u_{i,j}|^2\right)^{1/2}}{\left(\sum_{i=1}^{I}\sum_{j=1}^{J}|u_{i,j}|^2\right)^{1/2}}, \qquad \|e\|_{\infty,\mathrm{rel}} = \frac{\max\limits_{\substack{1\le i\le I\\ 1\le j\le J}}|\tilde{u}_{i,j} - u_{i,j}|}{\max\limits_{\substack{1\le i\le I\\ 1\le j\le J}}|u_{i,j}|}, \tag{3.19}$$

where $u_{i,j}$ denotes the exact solution evaluated at the grid point (x_i, p_j).

Robustness is evaluated through a Monte Carlo study with $N_{\mathrm{MC}} = 50$ independent trials for each noise level δ. Following a standard practice in inverse and data-driven problems, we perturb the measured boundary data by additive Gaussian noise scaled by the signal magnitude [46, 47]:

$$\mathcal{D}^{\delta} = \mathcal{D} + \delta\,\mathrm{RMS}(\mathcal{D})\,\xi,$$

where $\mathcal{D}$ denotes the boundary derivative data (e.g., g_L, g_R, h_B, h_T) as well as the interior measurement $u_1 = u(x_0, p_0)$, ξ is a standard Gaussian random variable sampled independently for each trial and for each boundary grid location, and $\mathrm{RMS}(\mathcal{D})$ denotes the root-mean-square magnitude of the corresponding clean data. For each δ, we report the sample mean (and, when relevant, the standard deviation) of the error measures and visualize the resulting noise-to-error dependence in log-log plots.

The reconstruction of $\tilde{\lambda}$ inherits errors mainly through the approximation of u_x and u_p from the discrete field $\tilde{u}$. In particular, we recover local derivatives at cell centers by differentiating the bilinear interpolant $P(x, p)$ built from neighboring nodal values. For sufficiently smooth u, standard interpolation estimates for Q_1 (bilinear) elements yield a second-order approximation in the function values and a first-order approximation in the derivatives, i.e., $\|u - P\| = O(h^2)$ and $\|\nabla u - \nabla P\| = O(h)$ (with $h = \max\{\Delta x, \Delta p\}$), up to constants depending on higher derivatives of u and mesh regularity. Accordingly, Tikhonov regularization improves the stability of the final inversion step, at the expense of a controllable smoothing bias governed by the parameter α.

The overall computational procedure, encompassing the numerical solution of $u(x, p)$ and the subsequent reconstruction of the source function $\lambda(x, p)$, is summarized in Algorithm 1.

Algorithm 1 Numerical computation of $u(x, p)$ and reconstruction of $\lambda(x, p)$

Require: Domain boundaries a, b, c, d, grid sizes I, J, functions H, β, K, F, boundary data g_L, g_R, h_B, h_T, and the derivative of the unknown function λ_x at the boundaries.

Ensure: Numerical solution $\tilde{u}_{i,j}$ and reconstructed $\tilde{\lambda}_{i,j}$.

Step 1: Grid initialization

Define step sizes $\Delta x = \frac{b-a}{I+1}$ and $\Delta p = \frac{d-c}{J+1}$.

Generate mesh points $x_i = a + i\Delta x$ and $p_j = c + j\Delta p$.

Compute trapezoidal weights w_ℓ for $\ell = 0, \ldots, J+1$.

Step 2: Coefficient computation

Compute symbolic derivatives of $H(x, p)$ and $\beta(x, p)$ to obtain H_p, H_x, H_{pp}, H_{xx}, H_{ppx}, β_p, β_x, β_{xp}.

Evaluate coefficients $k_1(i, j)$ through $k_{10}(i, j)$ at each grid node (x_i, p_j) as defined in Eq (3.6).

Step 3: Matrix assembly and system formulation

Construct the block tridiagonal matrix Λ_1 and sparse coefficient matrix Λ_2 using sub-blocks $\mathcal{M}_1^{(i)}$, $\mathcal{M}_2^{(i)}$ and $\mathcal{M}_3^{(i)}$ as defined in (3.10)–(3.12).

Compute the dense matrices $\mathcal{M}_4^{(i)}$ and $\mathcal{M}_5^{(i)}$ representing the integral contributions k_7 and k_8, and assemble Λ_3 from these blocks.

Assemble the complete coefficient matrix $\Lambda = \Lambda_1 + \Lambda_2 + \Lambda_3$.

Formulate the source vector $\mathbf{G}$ by evaluating $(F_{xp})_{i,j}$ at all internal mesh points.

Step 4: Boundary conditions

Eliminate ghost nodes using second-order one-sided formulas for g_L, g_R, h_B, h_T.

Update the first and last rows/blocks of Λ and the vector $\mathbf{b}$ to incorporate non homogeneous data.

Step 5: Linear system solution for u

Solve the sparse matrix equation $\Lambda\tilde{\mathbf{u}} + \mathbf{b} = \mathbf{G}$.

Reshape the solution vector $\tilde{\mathbf{u}}$ to the $I \times J$ grid.

Step 6: Computation of auxiliary function λ^{pre}

Compute numerical approximations of the derivatives $\tilde{u}_x$ and $\tilde{u}_p$ by differentiating the bilinear interpolant $P(x, p)$ fitted to the four corner values of each cell (i, j).

Approximate the integral term $\mathcal{I}(\tilde{u})_{i,j} = \int_c^d K(x_i, p_j, p')\,\tilde{u}(x_i, p')\,dp'$ using the trapezoidal rule.

Evaluate $\lambda_{i,j}^{\text{pre}} = (H_p\tilde{u}_x - H_x\tilde{u}_p)_{i,j} + (\beta\tilde{u})_{i,j} + \mathcal{I}(\tilde{u})_{i,j} - F_{i,j}$ at all grid points.

Step 7: Reconstruction of $\tilde{\lambda}(x, p)$

Assume the separation form $\lambda(x, p) = \rho(x) + \mu(p)$.

Formulate the overdetermined system $\mathbf{Tz} \approx \mathbf{y}$, where $\mathbf{y}$ collects the values $\lambda_{i,j}^{\text{pre}}$ over all cell centers.

Define the unknown vector $\mathbf{z} = [\rho(x_1), \ldots, \rho(x_I), \mu(p_1), \ldots, \mu(p_J)]^T$.

Add Tikhonov regularization (e.g., $\rho''(x) \approx 0, \mu''(p) \approx 0$) to the matrix $\mathbf{T}$.

Construct the final reconstructed function: $\tilde{\lambda}_{i,j} = \rho(x_i) + \mu(p_j)$.

4. Numerical examples and discussion

In this section, we demonstrate the efficiency and high-order accuracy of the proposed computational framework through a detailed numerical example. The algorithm's performance is evaluated by comparing the numerical approximations $\tilde{u}$ and $\tilde{\lambda}$ with their respective exact analytical solutions.

Example 1. *Consider the problem of finding the pair* (u, λ) *in* $\Omega = (-1, 1) \times (-1, 1)$ *for Eq* (2.1)*, where*

$$H(x, p) = xp + p^2, \quad \beta(x, p) = 1 + xp,$$

the kernel function is

$$K(x, p, p') = \left(1 + \frac{1}{2}\sin(x)\right)(p - p')^2,$$

and the function $F(x, p)$ *is given by*

$$\begin{aligned} F(x, p) = {} & (p^2 - 0{,}035\, x \sin(x^2))\,(2p + x) - \cos(p^3) + (px + 1)(\sin(p) + \cos(x^2) + p^2 x) \\ & - p(0{,}017\cos(p) + 2px) + 0{,}5\, x^2 \\ & + (\sin(x) + 2)(0{,}2\, x + 0{,}3\cos(x^2) + 0{,}3\, p^2 x + p^2\cos(x^2) - 0{,}012\, p). \end{aligned}$$

The boundary conditions are

$$\begin{aligned} & u_x(-1, p) = p^2 + \sin(1), \qquad u_x(1, p) = p^2 - \sin(1), \\ & u_p(x, -1) = \cos(1) - 2x, \qquad u_p(x, 1) = 2x + \cos(1), \\ & \lambda_x(-1, p) = 1, \qquad \lambda_x(1, p) = -1, \end{aligned}$$

and the interior condition is $u(0, 0) = 1$.

The exact solution of the problem is

$$u(x, p) = \cos(x^2) + xp^2 + \sin(p), \quad \lambda(x, p) = -\frac{x^2}{2} + \cos(p^3).$$

The accuracy of the proposed method is quantified in Tables 1 and 2, which summarize the error norms for $u(x, p)$ and the reconstructed source term $\lambda(x, p)$, respectively; here, CR_∞ denotes the observed convergence rate computed from $\|e\|_{\infty,\mathrm{rel}}$ across two consecutive grid levels, and $\kappa(\tilde{\Lambda})$ denotes the estimated condition number of the matrix $\tilde{\Lambda}$. The CPU times reported in Table 2 reflect the increasing cost of the dense integral operator as the grid is refined.

Table 1. Numerical error metrics and matrix condition numbers for the solution $u(x, p)$.

Grid	$\|e\|_\infty$	$\|e\|_{\infty,\mathrm{rel}}$	CR_∞	$\|e\|_{2,\mathrm{rel}}$	$\kappa(\tilde{\Lambda})$
40×40	8.66×10^{-4}	4.29×10^{-4}	—	4.97×10^{-4}	1.35×10^{8}
80×80	2.13×10^{-4}	1.05×10^{-4}	2.03	1.20×10^{-4}	6.00×10^{9}
100×100	1.36×10^{-4}	6.72×10^{-5}	2.00	7.65×10^{-5}	2.01×10^{10}
150×150	5.99×10^{-5}	2.97×10^{-5}	2.00	3.37×10^{-5}	1.33×10^{11}

Table 2. Numerical error metrics for the reconstructed function $\tilde{\lambda}(x, p)$.

Grid	$\|e_\lambda\|_\infty$	CR_∞	$\|e_\lambda\|_{2,\mathrm{rel}}$	CPU (s)
40×40	1.37×10^{-2}	—	6.06×10^{-3}	1.94
80×80	3.44×10^{-3}	1.99	1.44×10^{-3}	20.52
100×100	2.19×10^{-3}	2.01	9.14×10^{-4}	69.47
150×150	9.89×10^{-4}	2.00	4.01×10^{-4}	369.47

The accuracy of the proposed method is visually assessed in Figures 1–11, where the numerical solutions for u and λ are compared with their exact counterparts through surface plots, cross-sections, and error analyses using a spatial and velocity discretization of 80×80.

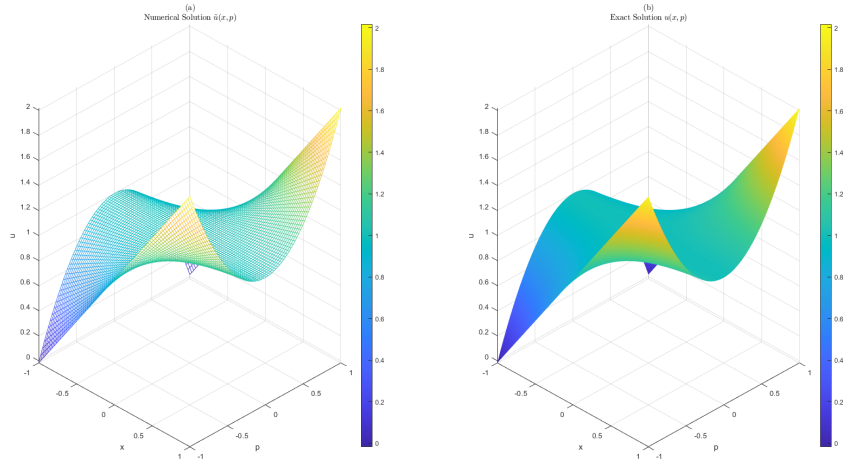

Figure 1. Comparison of (a) the numerical solution $\tilde{u}(x, p)$ and (b) the exact solution $u(x, p)$.

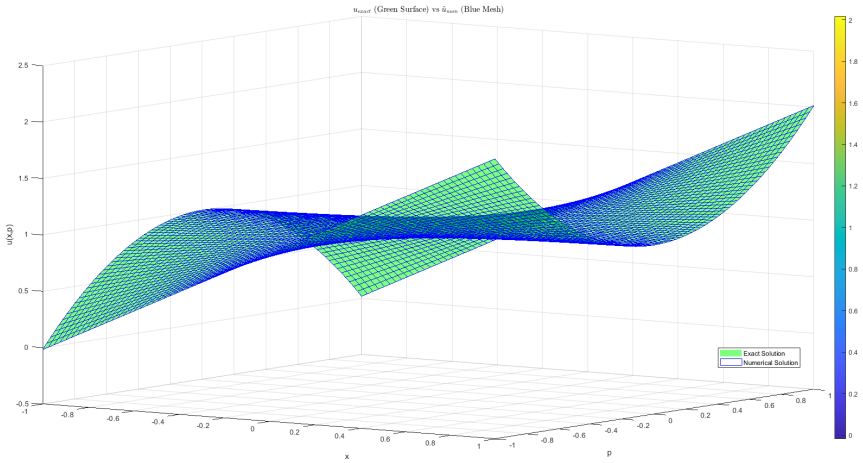

Figure 2. Overlay comparison: exact solution u_{exact} (green surface) and numerical solution $\tilde{u}_{num}$ (blue mesh).

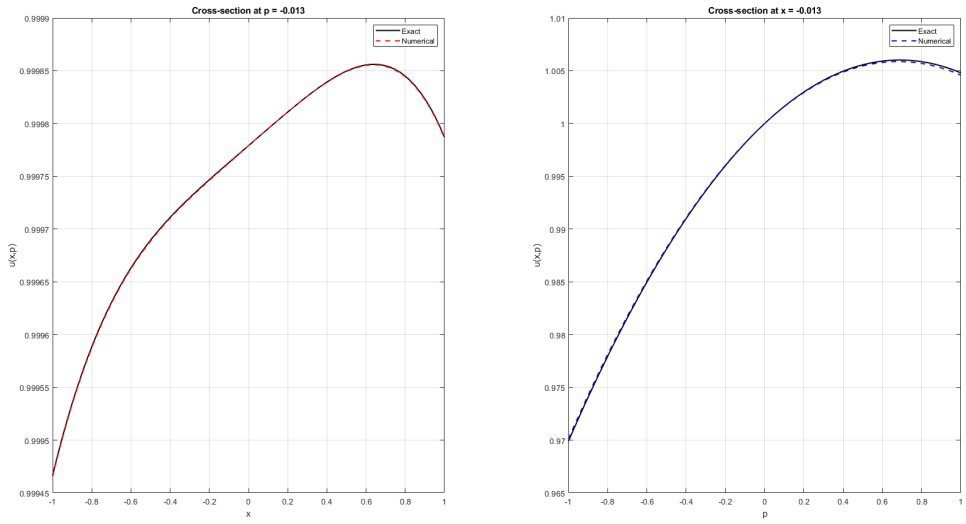

Figure 3. Cross-sectional profiles of $u(x, p)$ at fixed $p = -0.013$ (left) and $x = -0.013$ (right).

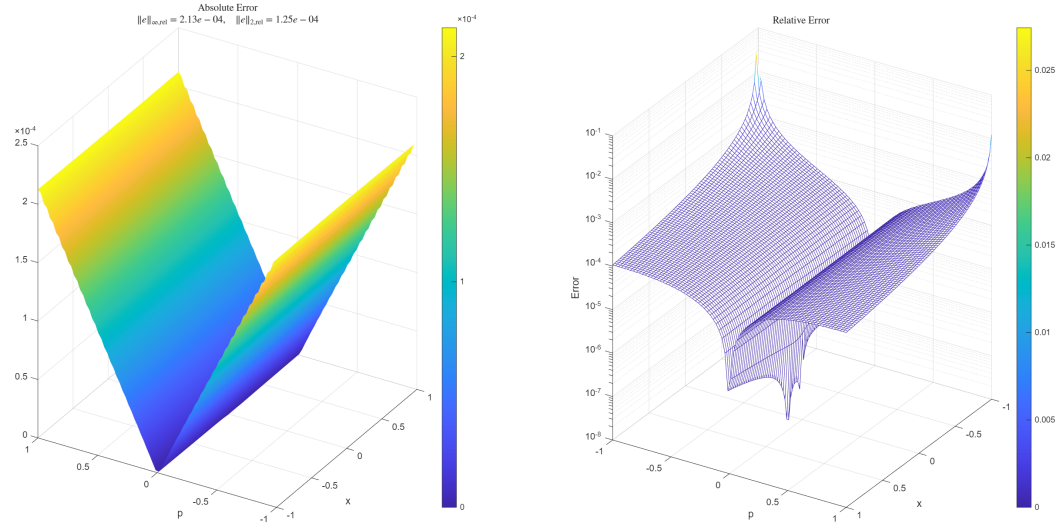

Figure 4. Error analysis for $u(x, p)$: absolute error (left) and relative error in log scale (right).

The average $\|e\|_\infty$ and $\|e\|_2$ errors grow linearly with δ on the log-log scale, closely tracking the theoretical bound $\sim \kappa(\tilde{\Lambda}) \cdot \delta$, which confirms the stability of the forward solver under boundary data perturbations. The horizontal dashed lines indicate the baseline discretization errors at $\delta = 0$. See Figure 5 for the Monte Carlo noise-sensitivity results, and Figure 6 for the L-curve based selection of the Tikhonov regularization parameter.

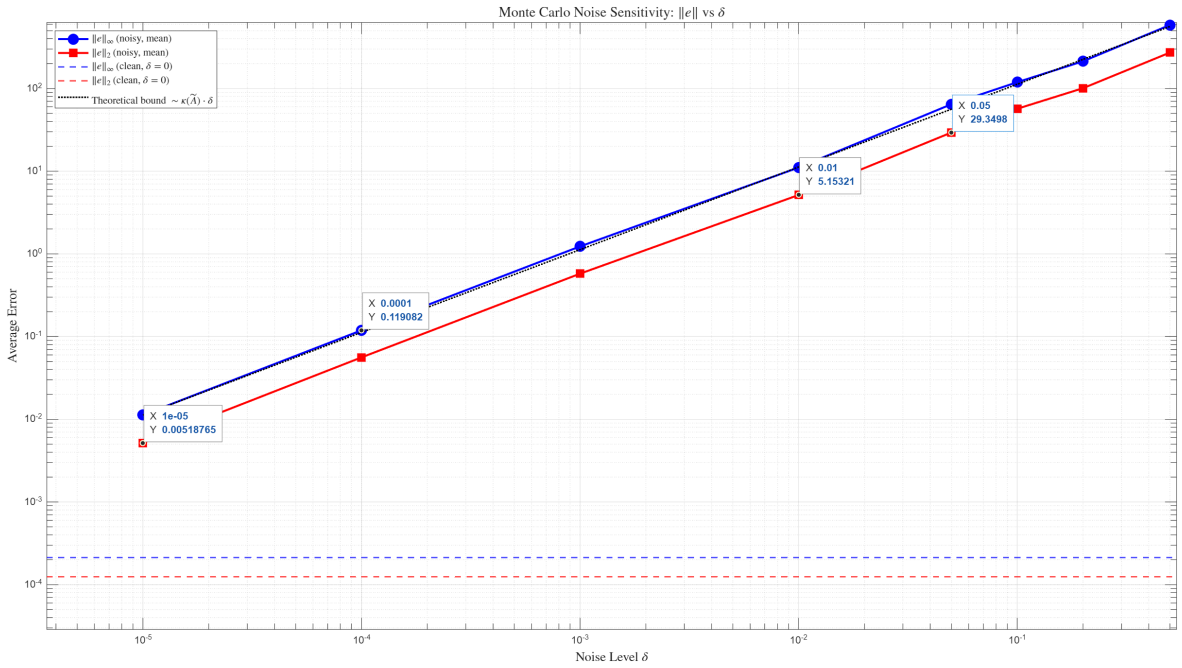

Figure 5. Monte Carlo noise sensitivity for $\tilde{u}$ ($N_{\mathrm{MC}} = 50$ trials): sample-mean $\|e\|_\infty$ (blue) and $\|e\|_2$ (red) vs. δ; dashed lines show the $\delta = 0$ baseline; dotted curve is the theoretical bound $\sim \kappa(\tilde{A}) \cdot \delta$.

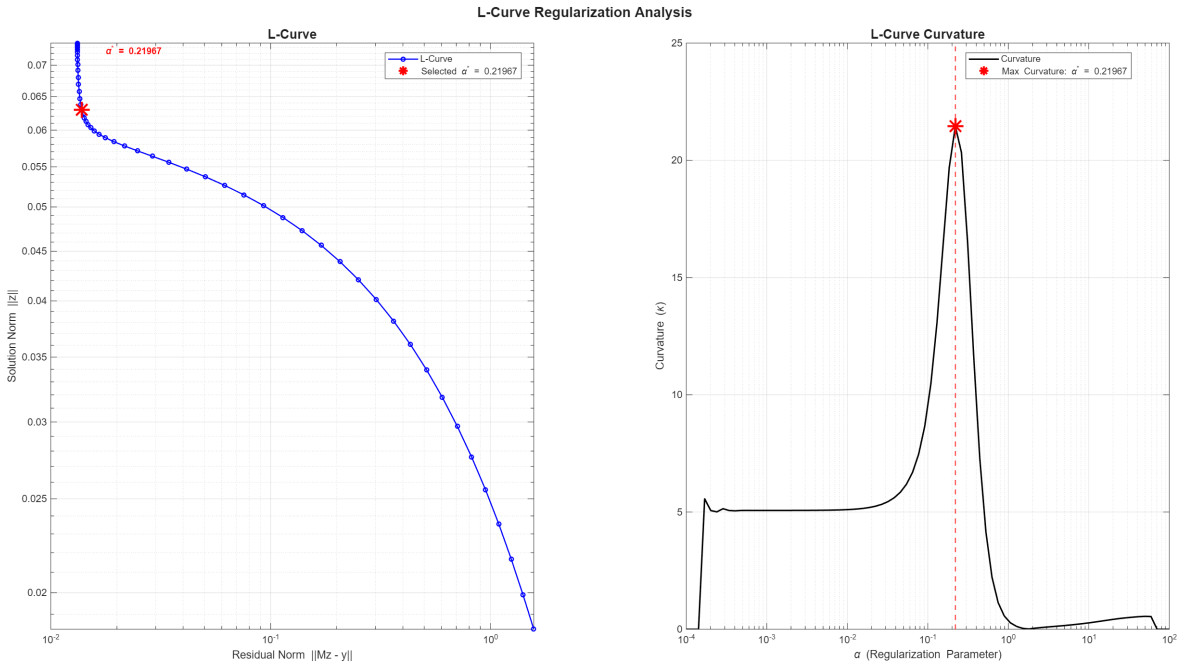

Figure 6. Selection of the Tikhonov regularization parameter α via the L-curve criterion.

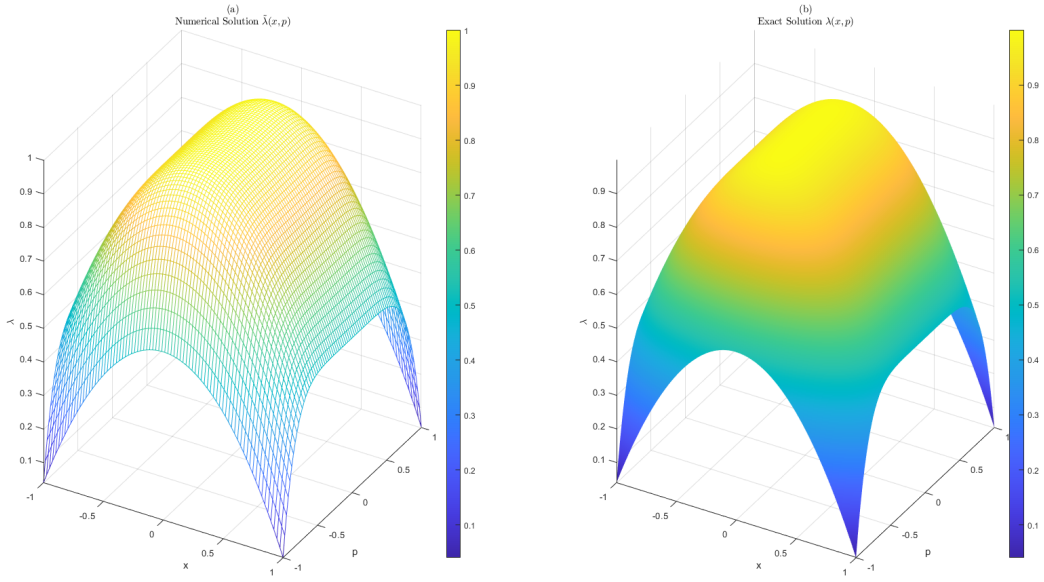

Figure 7. Comparison of the numerical solution $\tilde{\lambda}(x, p)$ (left) and the exact solution $\lambda(x, p)$ (right).

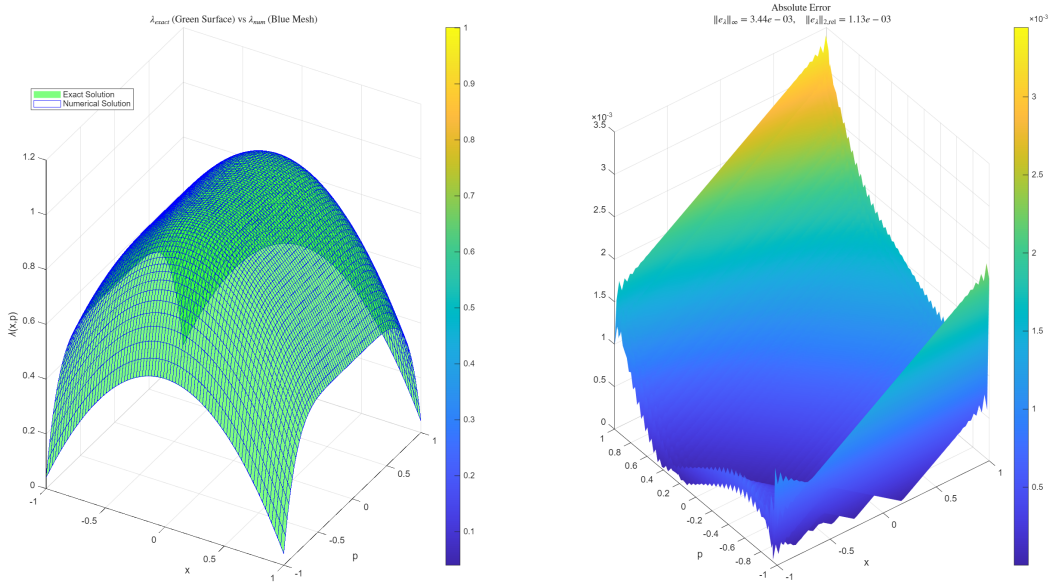

Figure 8. Comparison of λ_{exact} vs λ_{num} (left) and the absolute error map for λ (right).

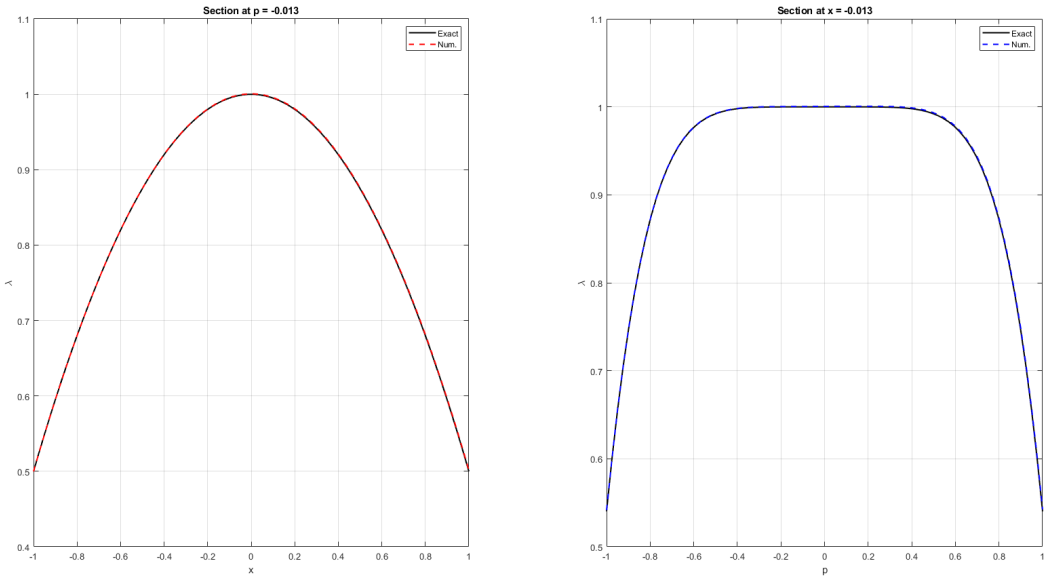

Figure 9. Cross-sectional profiles of λ at fixed $p = -0.013$ (left) and $x = -0.013$ (right).

This is further supported by Figure 10, which presents the correlation analysis between the numerical and exact values, and Figure 11, which illustrates the convergence rate of the maximum absolute error.

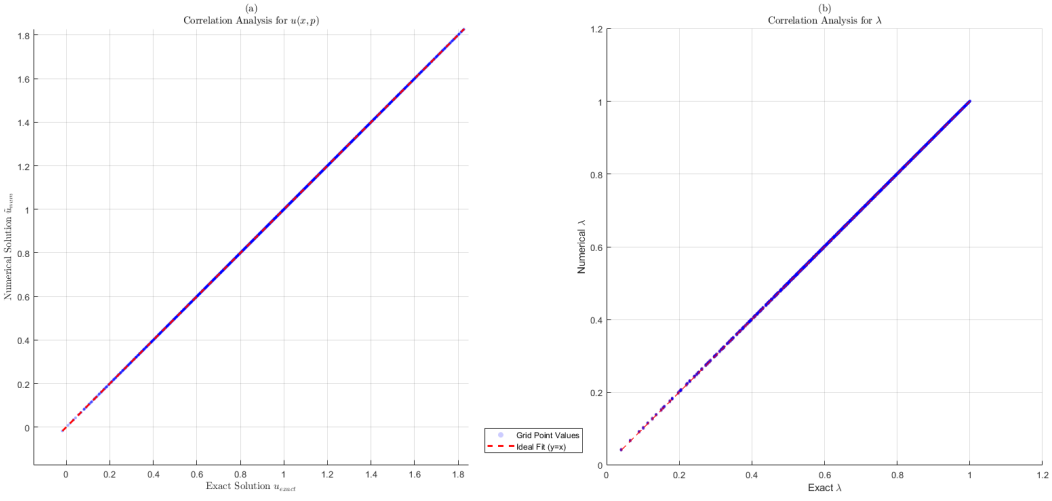

Figure 10. Correlation analysis: numerical vs. exact values for $u(x, p)$ (left) and λ (right).

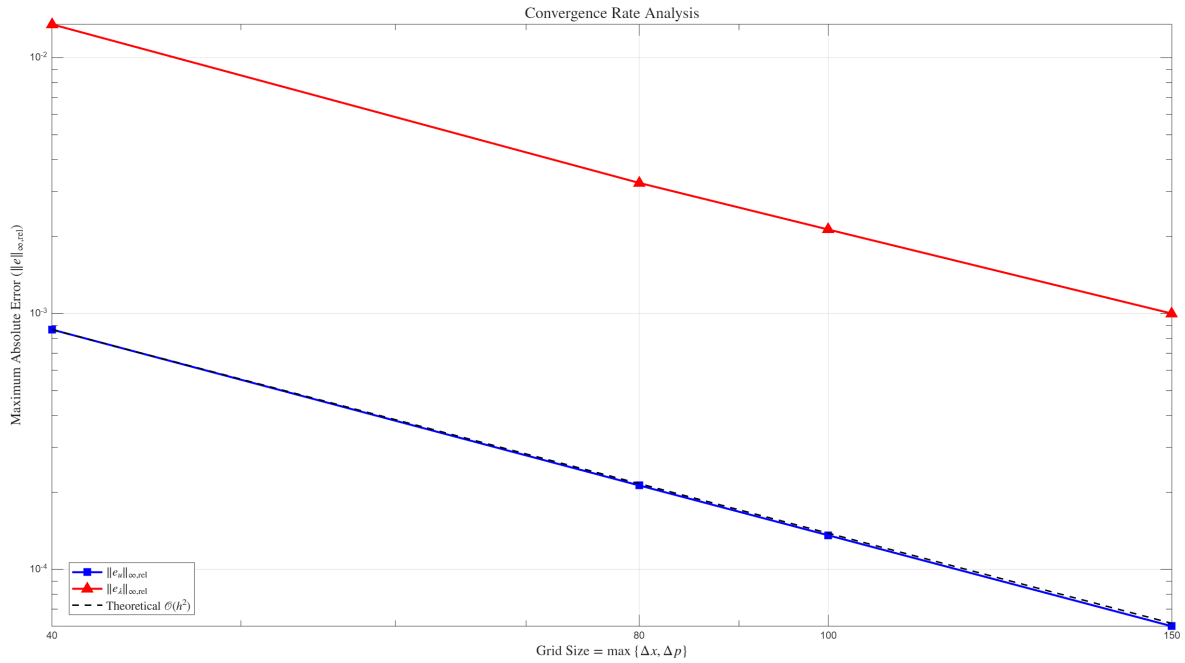

Figure 11. Convergence rate analysis showing $\|e\|_{\infty,\mathrm{rel}}$ versus $h = \max\{\Delta x, \Delta p\}$ for u and λ.

Example 2. *Consider the problem of finding the pair* (u, λ) *in* $\Omega = (0.1, 2)\times(0.1, 2)$ *for eq* (2.1)*, where*

$$H(x, p) = x + p^2, \quad \beta(x, p) = x^2 + p^2,$$

the kernel function is $K(x, p, p') = x(p - p')$*, and the function* $F(x, p)$ *is given by*

$$\begin{aligned} F(x,p) = (p^2+x^2)\Big(\cos(\pi x) + \sin(\pi p) + e^{-(p^2+x^2)} + 3\Big) - 4.14\,\cos(\pi p) - \sin(\pi x) - 5.34\,x \\ + 5.68\,px - 2p\Big(\pi\sin(\pi x) + 2x\,e^{-(p^2+x^2)}\Big) + 2p\,e^{-(p^2+x^2)} - 1.99\,x\cos(\pi x) - 0.48\,x\,e^{-x^2} \\ + 0.78\,px\,e^{-x^2} + 1.9\,px\cos(\pi x) - 3. \end{aligned}$$

The boundary conditions are

$$\begin{aligned} &u_x(0.1, p) = -0.2e^{-(p^2+0.01)} - \pi\sin(0.1\pi), \qquad u_x(2, p) = -4e^{-(p^2+4)}, \\ &u_p(x, 0.1) = -0.2e^{-(0.01+x^2)} + \pi\cos(0.1\pi), \qquad u_p(x, 2) = -4e^{-(4+x^2)} - \pi, \\ &\lambda_x(0.1, p) = \pi\cos(0.1\pi), \qquad \lambda_x(2, p) = \pi, \end{aligned}$$

and the interior condition is $u(1, 1) = 2.1353$.

The exact solution of the problem is

$$\begin{aligned} u(x, p) &= 3 + \cos(\pi x) + e^{-(p^2+x^2)} + \sin(\pi p), \\ \lambda(x, p) &= 3 + \sin(\pi x) + \cos(\pi p). \end{aligned}$$

Tables 3 and 4 present the error metrics for $\tilde{u}$ and the reconstructed $\tilde{\lambda}$, respectively. Both quantities converge at the expected rate of $O(h^2)$, with $\mathrm{CR}_\infty \approx 2$ across all refinement levels.

Table 3. Numerical error metrics and matrix condition numbers for the solution $u(x, p)$.

Grid	$\|e\|_\infty$	$\|e\|_{\infty,\text{rel}}$	CR_∞	$\|e\|_{2,\text{rel}}$	$\kappa(\tilde{\Lambda})$
40×40	1.21×10^{-2}	2.10×10^{-3}	—	1.20×10^{-3}	6.63×10^{6}
80×80	2.33×10^{-3}	4.05×10^{-4}	2.33	2.34×10^{-4}	1.47×10^{8}
100×100	1.43×10^{-3}	2.49×10^{-4}	2.16	1.46×10^{-4}	3.86×10^{8}
150×150	5.95×10^{-4}	1.04×10^{-4}	2.15	5.98×10^{-5}	1.89×10^{9}

Table 4. Numerical error metrics for the reconstructed function $\tilde{\lambda}(x, p)$.

Grid	$\|e_\lambda\|_\infty$	CR_∞	$\|e_\lambda\|_{2,\text{rel}}$	CPU (s)
40×40	1.21×10^{-1}	—	7.70×10^{-3}	4.43
80×80	2.57×10^{-2}	2.21	1.56×10^{-3}	22.93
100×100	1.60×10^{-2}	2.07	9.67×10^{-4}	66.20
150×150	6.67×10^{-3}	2.16	3.98×10^{-4}	1410.15

For Example 2, the performance of the proposed method is illustrated through surface plots in Figures 12–22. Cross-sectional comparisons are presented in Figures 14 and 20. The corresponding absolute error visualizations are shown in Figures 15 and 21. All results are obtained on an 80×80 spatial–velocity grid.

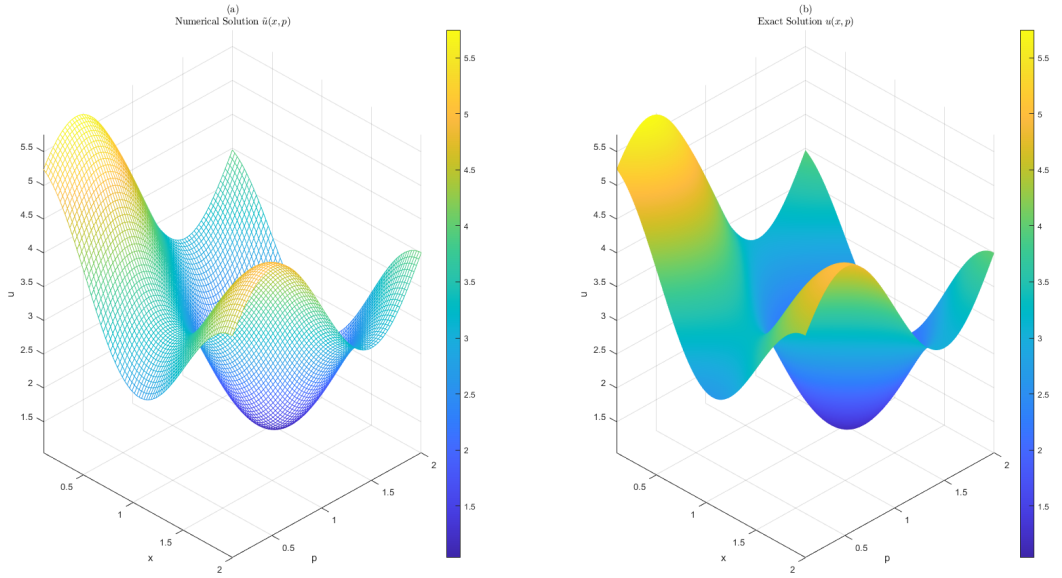

Figure 12. Comparison of (a) the numerical solution $\tilde{u}(x, p)$ and (b) the exact solution $u(x, p)$.

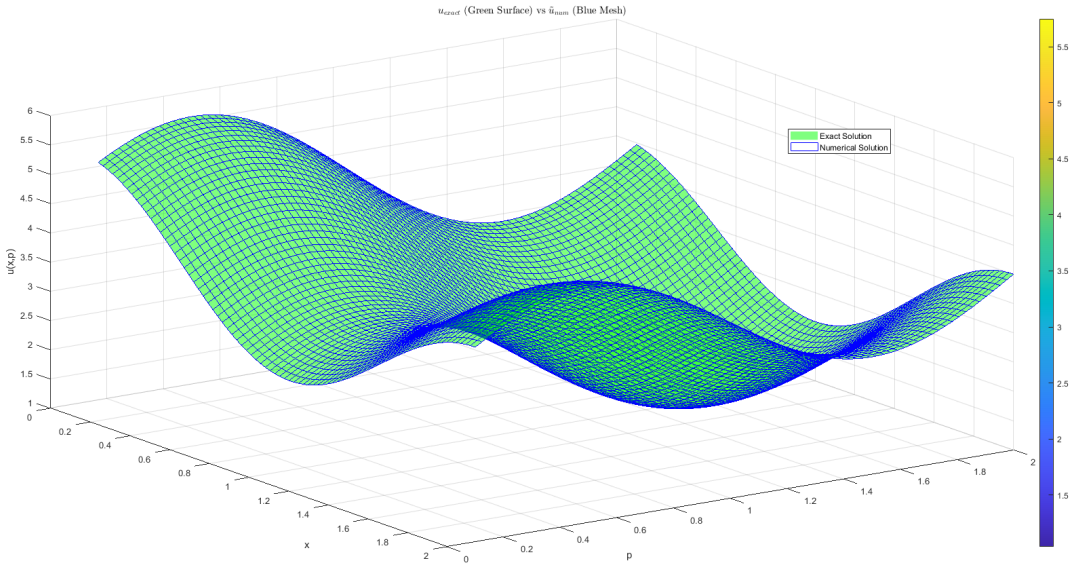

Figure 13. Overlay comparison: exact solution u (green surface) vs. numerical solution $\tilde{u}$ (blue mesh).

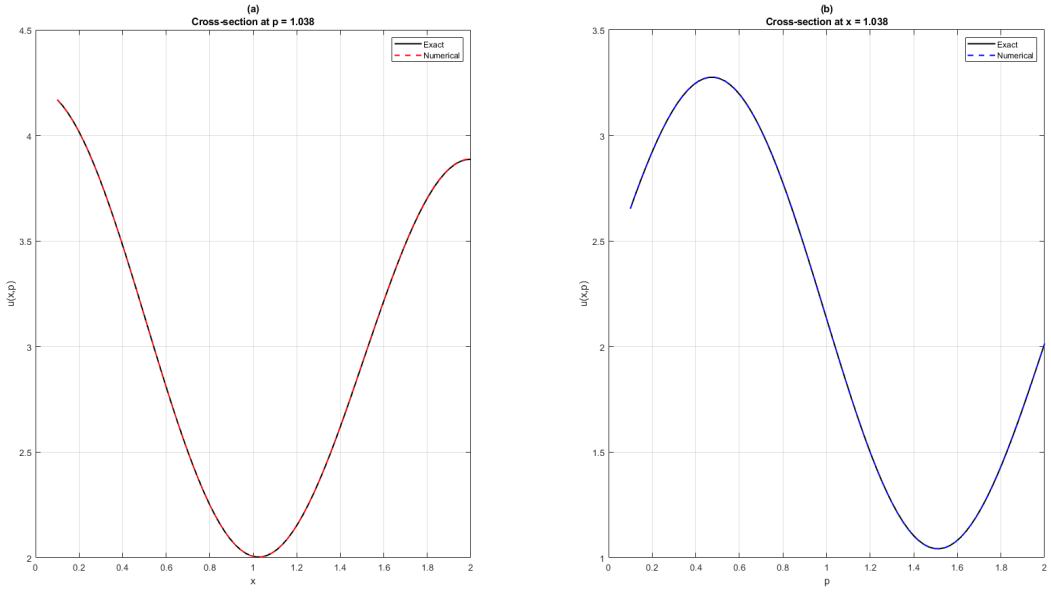

Figure 14. Cross-sectional profiles of $u(x, p)$ at fixed $p = -0.013$ (left) and $x = -0.013$ (right).

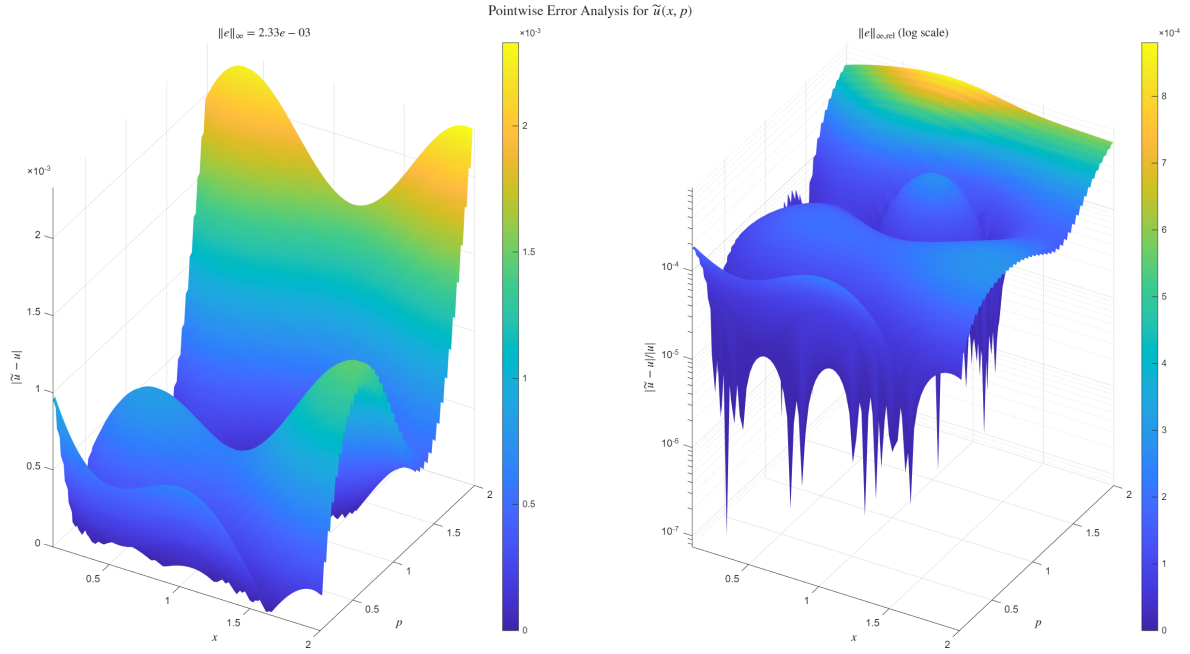

Figure 15. Pointwise error maps for $\tilde{u}(x, p)$: absolute error $|\tilde{u} - u|$ (left) and relative error $|\tilde{u} - u|/|u|$ in log scale (right).

The average $\|e\|_{\infty,\mathrm{rel}}$ and $\|e\|_{2,\mathrm{rel}}$ errors grow approximately linearly with δ on the log–log scale (Figure 16). The Tikhonov regularization parameter α is selected using the L-curve criterion (Figure 17).

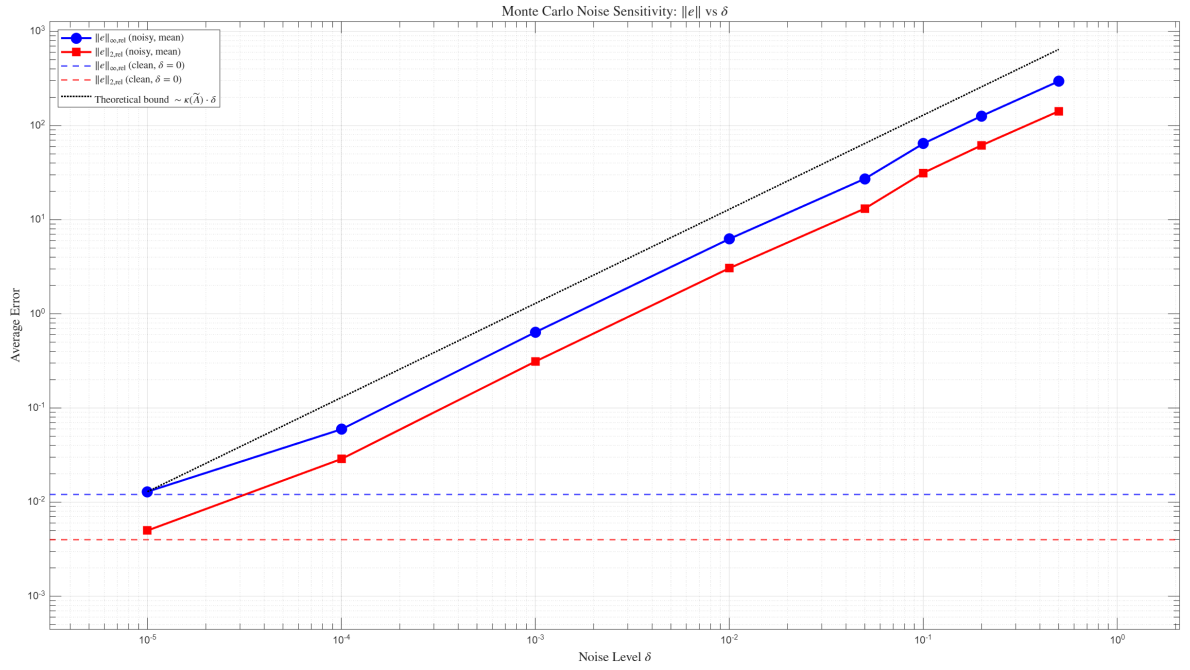

Figure 16. Monte Carlo noise sensitivity analysis for $\tilde{u}$ ($N_{\mathrm{MC}} = 50$ trials per noise level δ).

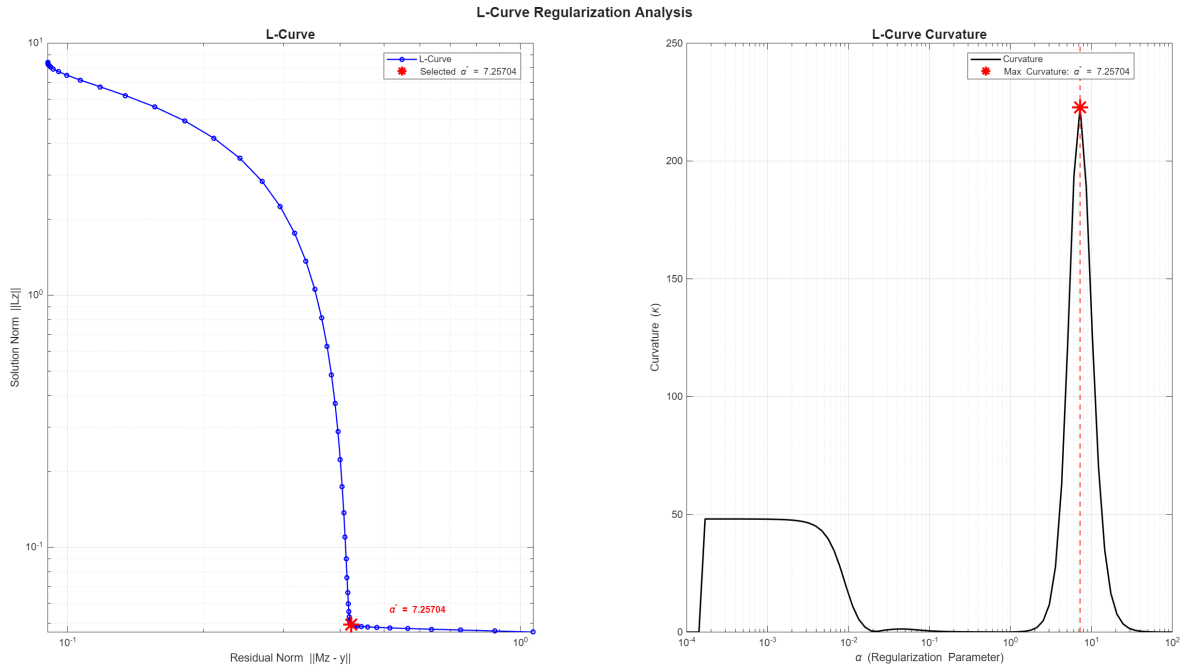

Figure 17. Selection of the Tikhonov regularization parameter α via the L-curve criterion.

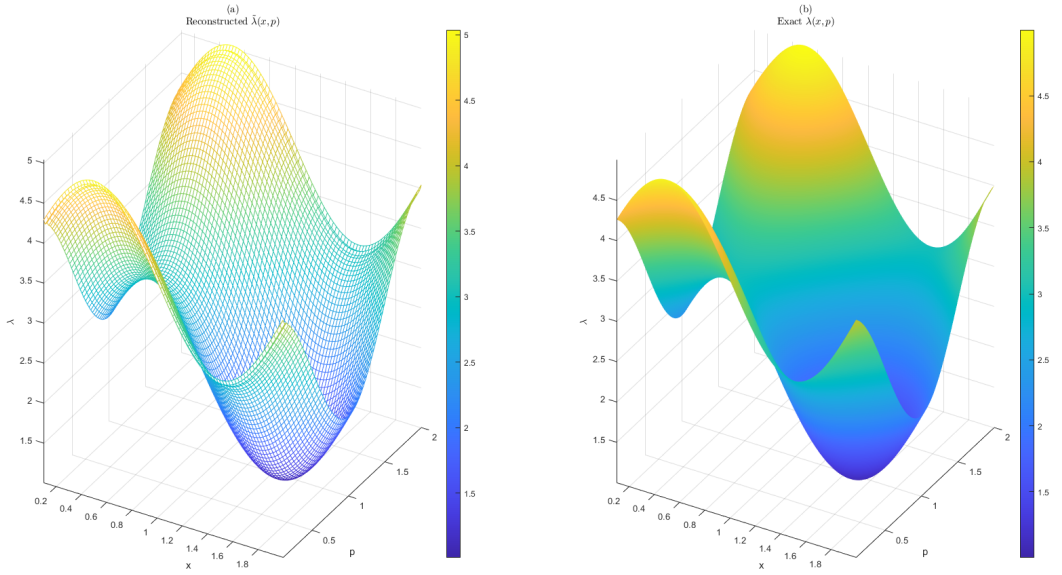

Figure 18. Comparison of the numerical solution $\tilde{\lambda}(x, p)$ (left) and the exact solution $\lambda(x, p)$ (right).

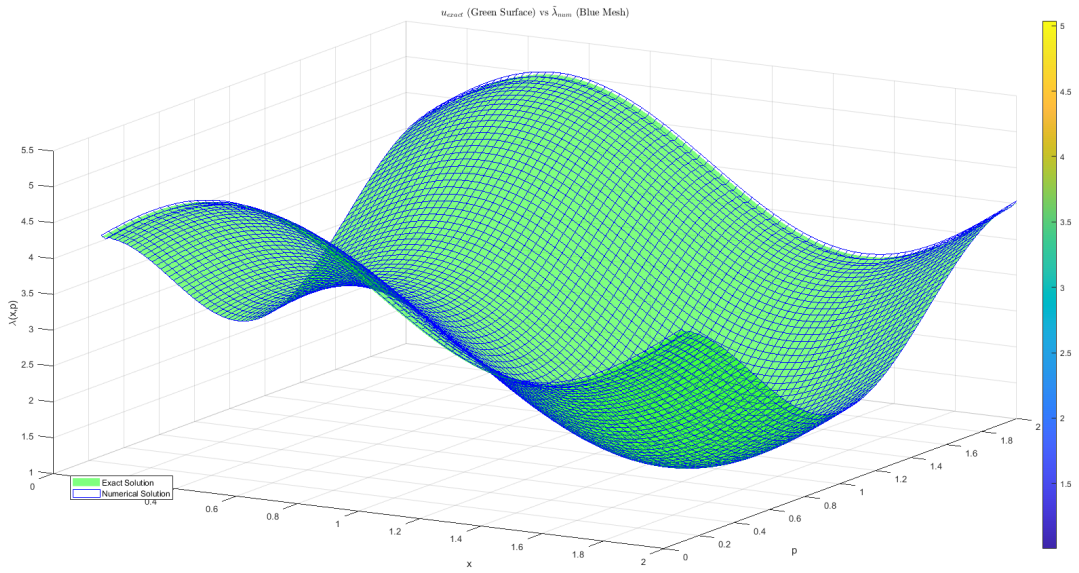

Figure 19. Comparison of λ vs. $\tilde{\lambda}$ (left) and the absolute error map for λ (right).

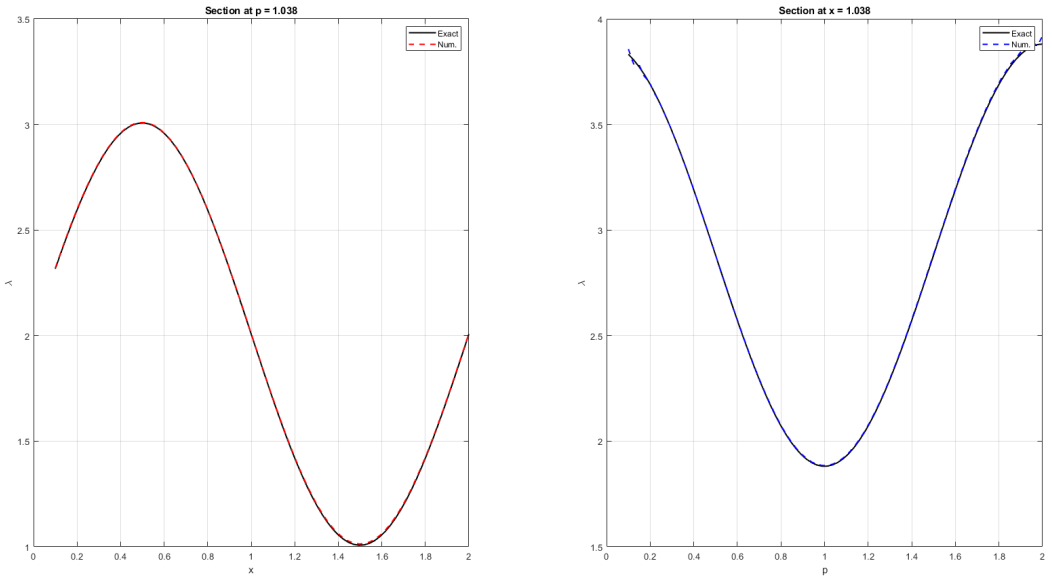

Figure 20. Cross-sectional profiles of λ at fixed $p = -0.013$ (left) and $x = -0.013$ (right).

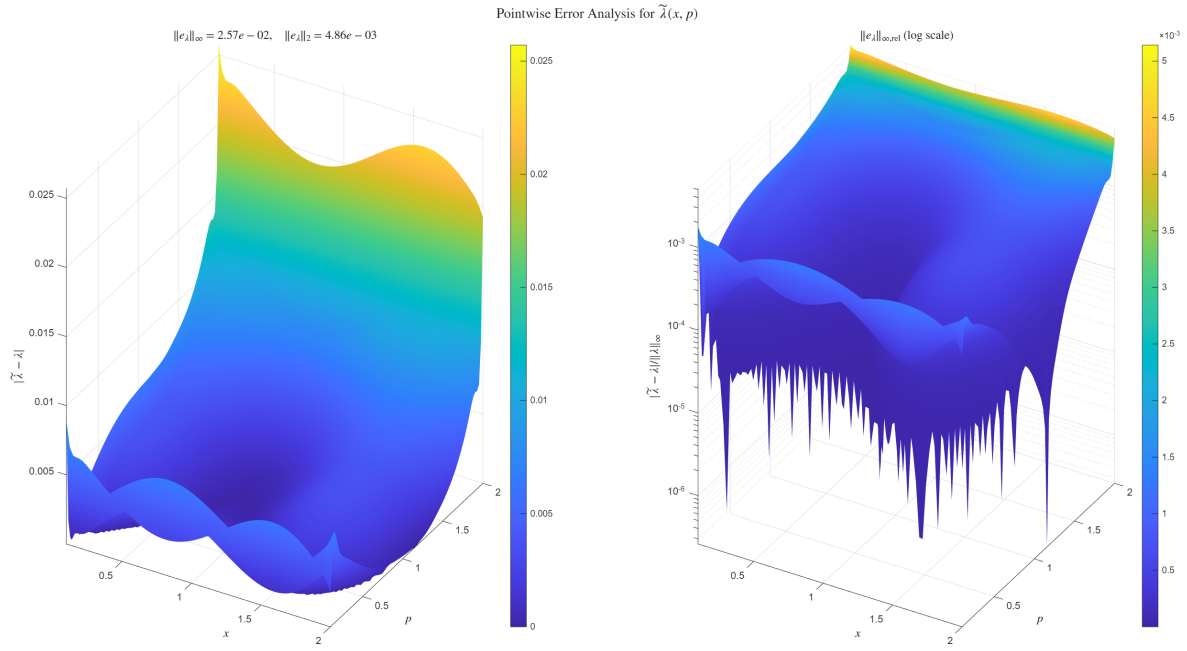

Figure 21. Pointwise error maps for $\tilde{\lambda}$: absolute error $|\tilde{\lambda} - \lambda|$ (left) and relative error $|\tilde{\lambda} - \lambda|/\|\lambda\|_\infty$ in log scale (right).

Additional evidence is provided by Figure 22, which reports the correlation between the numerical and exact results.

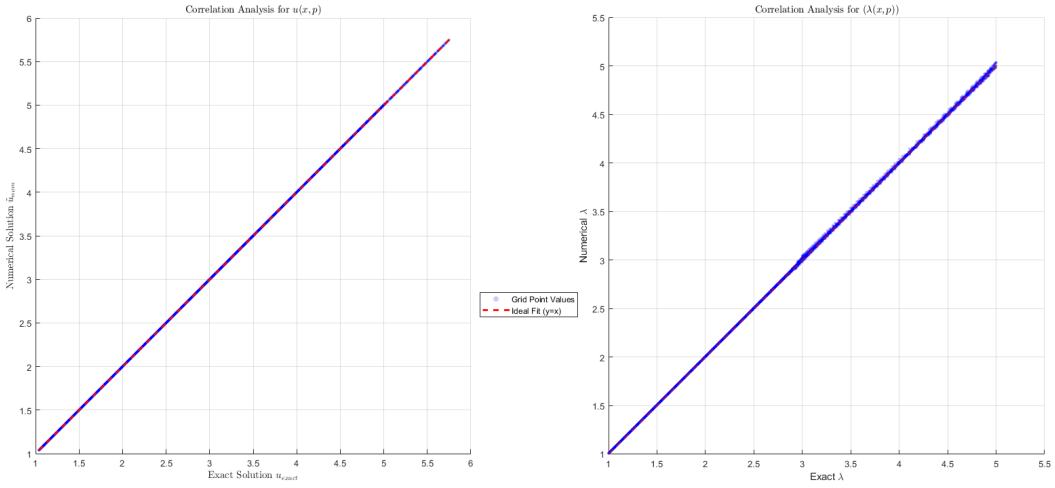

Figure 22. Correlation analysis: numerical vs exact values for $u(x, p)$ (left) and λ (right).

5. Conclusions

In this work, we propose an algorithm for the numerical recovery of an unknown source in a stationary kinetic equation with absorption and scattering. The primary contributions of this study are establishing the uniqueness of the solution and developing a robust numerical reconstruction method utilizing boundary conditions and interior point data.

Our numerical framework is based on finite difference approximations for the derivatives and the trapezoidal rule for the discretization of the scattering term. The reconstruction of the unknown source function $\lambda(x, p)$ is achieved using a bilinear interpolation strategy coupled with Tikhonov regularization. The efficiency of this method is validated through detailed numerical experiments.

Consequently, the proposed computational strategy provides a promising framework for future applications to direct and inverse problems involving time-dependent higher-order models and multidimensional geometries; moreover, extending the present approach to non-smooth boundary data with dedicated stabilization and regularization strategies remains an important topic for future work.

Use of AI tools declaration

The authors used AI-assisted tools solely for grammar correction and language editing. All mathematical ideas, results, proofs, and scientific content are entirely the authors' original work.

Conflict of interest

The authors declare there are no conflicts of interest.

References

1. C. Cercignani, R. Illner, M. Pulvirenti, *The Mathematical Theory of Dilute Gases*, Springer Science & Business Media, New York, 2013. https://doi.org/10.1007/978-1-4419-8524-8
2. C. Villani, *Topics in Optimal Transportation*, American Mathematical Soc., 2003.
3. B. Perthame, *Transport Equations in Biology*, Birkhäuser Basel, 2007. https://doi.org/10.1007/978-3-7643-7842-4
4. F. Golse, On the dynamics of large particle systems in the mean field limit, in *Macroscopic and Large Scale Phenomena: Coarse Graining, Mean Field Limits and Ergodicity*, Springer Cham, (2016), 1–144. https://doi.org/10.1007/978-3-319-26883-5_1
5. L. Saint-Raymond, *Hydrodynamic Limits of the Boltzmann Equation*, Springer, New York, 2009. https://doi.org/10.1007/978-3-540-92847-8
6. Z. Jin, R. Li, Natural model reduction for kinetic equations, *Res. Math. Sci.*, **11** (2024), 53. https://doi.org/10.1007/s40687-024-00466-7
7. G. A. Bird, *Molecular Gas Dynamics and the Direct Simulation of Gas Flows*, Oxford University Press, 1994.

8. Y. Yin, X. Tian, X. Zhu, H. Liu, X. Zhang, C. Zhu, et al., Fluid dynamics of gas–liquid slug flow under the expansion effect in a microchannel, *Chem. Eng. Sci.*, **302** (2025), 120941. https://doi.org/10.1016/j.ces.2024.120941
9. Y. Sone, *Molecular Gas Dynamics: Theory, Techniques, and Applications*, Birkhäuser Boston, 2007. https://doi.org/10.1007/978-0-8176-4573-1
10. D. R. Nicholson, *Introduction to Plasma Theory*, Wiley, New York, 1983.
11. R. D. Hazeltine, *The Framework of Plasma Physics*, CRC Press, 2018.
12. S. Chandrasekhar, *Radiative Transfer*, Courier Corporation, 2013.
13. E. E. Lewis, W. F. Miller, *Computational Methods of Neutron Transport*, Wiley, 1983.
14. M. F. Modest, S. Mazumder, *Radiative Heat Transfer*, Academic Press, 2021.
15. A. A. Schekochihin, S. C. Cowley, W. Dorland, G. W. Hammett, G. G. Howes, E. Quataert, et al., Astrophysical gyrokinetics: Kinetic and fluid turbulent cascades in magnetized weakly collisional plasmas, *Astrophys. J. Suppl. Ser.*, **182** (2009), 310. https://doi.org/10.1088/0067-0049/182/1/310
16. I. G. Abel, G. G. Plunk, E. Wang, M. Barnes, S. C. Cowley, W. Dorland, et al., Multiscale gyrokinetics for rotating tokamak plasmas: Fluctuations, transport and energy flows, *Rep. Prog. Phys.*, **76** (2013), 116201. https://doi.org/10.1088/0034-4885/76/11/116201
17. P. L. Lions, T. Paul, Sur les mesures de Wigner, *Rev. Mat. Iberoam.*, **9** (1993), 553–618. https://doi.org/10.4171/rmi/143
18. P. Gérard, P. A. Markowich, N. J. Mauser, F. Poupaud, Homogenization limits and Wigner transforms, *Commun. Pure Appl. Math.*, **50** (1997), 323–379. https://doi.org/10.1002/(SICI)1097-0312(199704)50:4¡323::AID-CPA4¿3.0.CO;2-C
19. P. A. Markowich, C. A. Ringhofer, C. Schmeiser, *Semiconductor Equations*, Springer, New York, 1990. https://doi.org/10.1007/978-3-7091-6961-2
20. M. Lundstrom, Fundamentals of carrier transport, 2nd edn, *Meas. Sci. Technol.*, **13** (2002), 230. https://doi.org/10.1088/0957-0233/13/2/703
21. L. L. Salas, F. C. Silva, A. S. Martinez, A new point kinetics model for ADS-type reactor using the importance function associated to the fission rate as weight function, *Ann. Nucl. Energy*, **190** (2023), 109869. https://doi.org/10.1016/j.anucene.2023.109869
22. W. Shan, P. Zheng, Global boundedness of the immune chemotaxis system with general kinetic functions, *Nonlinear Differ. Equ. Appl.*, **30** (2023), 29. https://doi.org/10.1007/s00030-023-00840-4
23. M. Conte, M. Groppi, A. Tosin, Kinetic and macroscopic equations for action potential in neural networks, in *Problems in Mathematical Biophysics*, Springer Cham, (2024), 77–104. https://doi.org/10.1007/978-3-031-60773-8_5
24. A. K. Amirov, *Integral Geometry and Inverse Problems for Kinetic Equations*, VSP, Utrecht, 2001.
25. Y. E. Anikonov, *Inverse Problems for Kinetic and Other Evolution Equations*, VSP, Utrecht, 2001.
26. G. Bal, Inverse transport theory and applications, *Inverse Probl.*, **25** (2009), 053001. https://doi.org/10.1088/0266-5611/25/5/053001

27. M. V. Klibanov, S. E. Pamyatnykh, Global uniqueness for a coefficient inverse problem for the non-stationary transport equation via Carleman estimate, *J. Math. Anal. Appl.*, **343** (2008), 352–365. https://doi.org/10.1016/j.jmaa.2008.01.071

28. F. Gölgeleyen, M. Yamamoto, Stability for some inverse problems for transport equations, *SIAM J. Math. Anal.*, **48** (2016), 2319–2344. https://doi.org/10.1137/15M1038128

29. P. Cannarsa, G. Floridia, F. Gölgeleyen, M. Yamamoto, Inverse coefficient problems for a transport equation by local Carleman estimate, *Inverse Probl.*, **35** (2019), 105013. https://doi.org/10.1088/1361-6420/ab1c69

30. M. Machida, M. Yamamoto, Global Lipschitz stability in determining coefficients of the radiative transport equation, *Inverse Probl.*, **30** (2014), 035010. https://doi.org/10.1088/0266-5611/30/3/035010

31. A. K. Amirov, F. Gölgeleyen, Solvability of an inverse problem for the kinetic equation and a symbolic algorithm, *Comput. Model. Eng. Sci.*, **65** (2010), 179–190. https://doi.org/10.3970/cmes.2010.065.179

32. F. Gölgeleyen, A. Amirov, On the approximate solution of a coefficient inverse problem for the kinetic equation, *Math. Commun.*, **16** (2011), 283–298.

33. A. K. Amirov, F. Gölgeleyen, A. Rahmanova, An inverse problem for the general kinetic equation and a numerical method, *Comput. Model. Eng. Sci.*, **43** (2009), 131–147. https://doi.org/10.3970/cmes.2009.043.131

34. A. Amirov, Z. Ustaoğlu, B. Heydarov, Solvability of a two dimensional coefficient inverse problem for transport equation and a numerical method, *Transp. Theory Stat. Phys.*, **40** (2011), 1–22. https://doi.org/10.1080/00411450.2010.529980

35. A. Amirov, Z. Ustaoğlu, On the approximation methods for the solution of a coefficient inverse problem for a transport-like equation, *Comput. Model. Eng. Sci.*, **54** (2009), 283–299. https://doi.org/10.3970/cmes.2009.054.283

36. İ. Gölgeleyen, M. Hasdemir, A solution algorithm for an inverse source problem for the kinetic equation, *Int. J. Mod. Phys. C*, **33** (2022), 2250151. https://doi.org/10.1142/S0129183122501510

37. F. Gölgeleyen, İ. Gölgeleyen, M. Hasdemir, A hybrid solution method for an inverse problem for the general transport equation, *Comput. Math. Appl.*, **192** (2025), 172–188. https://doi.org/10.1016/j.camwa.2025.05.014

38. İ. Gölgeleyen, M. Hasdemir, Ö. Kaytmaz, A computational approach to an inverse source problem for a kinetic equation with gradient-type boundary data and an interior point observation, *Electron. Res. Arch.*, **34** (2026), 2136–2156. https://doi.org/10.3934/era.2026096

39. M. V. Klibanov, J. Li, L. H. Nguyen, Z. Yang, Convexification numerical method for a coefficient inverse problem for the radiative transport equation, *SIAM J. Imaging Sci.*, **16** (2023), 35–63. https://doi.org/10.1137/22M1509837

40. T. Liu, F. Soleymani, M. Z. Ullah, Solving multi-dimensional European option pricing problems by integrals of the inverse quadratic radial basis function on non-uniform meshes, *Chaos Solitons Fractals*, **185** (2024), 115156. https://doi.org/10.1016/j.chaos.2024.115156

41. T. Liu, T. Li, M. Z. Ullah, On five-point equidistant stencils based on Gaussian function with application in numerical multi-dimensional option pricing, *Comput. Math. Appl.*, **176** (2024), 35–45. https://doi.org/10.1016/j.camwa.2024.09.003

42. A. N. Tikhonov, V. Y. Arsenin, *Solutions of Ill-Posed Problems*, Winston Washington, 1977.

43. T. Liu, Porosity reconstruction based on Biot elastic model of porous media by homotopy perturbation method, *Chaos Solitons Fractals*, **158** (2022), 112007. https://doi.org/10.1016/j.chaos.2022.112007

44. T. Liu, Parameter estimation with the multigrid-homotopy method for a nonlinear diffusion equation, *J. Comput. Appl. Math.*, **413** (2022), 114393. https://doi.org/10.1016/j.cam.2022.114393

45. P. C. Hansen, Analysis of discrete ill-posed problems by means of the L-curve, *SIAM Rev.*, **34** (1992), 561–580. https://doi.org/10.1137/1034115

46. J. Kaipio, E. Somersalo, *Statistical and Computational Inverse Problems*, Springer, New York, 2005. https://doi.org/10.1007/b138659

47. C. R. Vogel, *Computational Methods for Inverse Problems*, SIAM, Philadelphia, 2002.

AIMS Press